

Quasicrystalline electronic states in twisted bilayers and the effects of interlayer and sublattice symmetries

J. A. Crosse^{1,2} and Pilkyung Moon^{1,2,3,4,*}

¹*Arts and Sciences, NYU Shanghai, Shanghai, China*

²*NYU-ECNU Institute of Physics at NYU Shanghai, Shanghai, China*

³*Department of Physics, New York University, New York, USA*

⁴*State Key Laboratory of Precision Spectroscopy, East China Normal University, Shanghai, China*

(Dated: December 1, 2020)

We study the electronic structure of quasicrystals composed of incommensurate stacks of atomic layers. We consider two systems: a pair of square lattices with a relative twist angle of $\theta = 45^\circ$ and a pair of hexagonal lattices with a relative twist angle of $\theta = 30^\circ$, with various interlayer interaction strengths. This constitutes every two-dimensional bilayer quasicrystal system. We investigate the resonant coupling governing the quasicrystalline order in each quasicrystal symmetry, and calculate the quasi-band dispersion. The resonant interaction emerges in bilayer quasicrystals if all the dominant interlayer interactions occur between the atomic orbitals that have the same magnetic quantum number. Thus, not only the quasicrystal composed of the widely studied graphene, but also those composed of transition metal dichalcogenides will exhibit the quasicrystalline states. We find that some quasicrystalline states, which are usually obscured by decoupled monolayer states, are more prominent, i.e., "exposed", in the systems with strong interlayer interaction. We also show that we can switch the states between quasicrystalline configuration and its layer components, by turning on and off the interlayer symmetry.

I. INTRODUCTION

When two hexagonal lattices are overlapped, one on top of the other at a twist angle $\theta = 30^\circ$, the atomic arrangement is mapped on to a quasicrystalline lattice, which is ordered but not periodic, with a 12-fold rotational symmetry [1]. Recently, it has been demonstrated that bilayer graphene with a precise rotation angle of 30° exhibits the atomic structures satisfying the quasicrystalline tiling as well as a spectrum respecting the 12-fold rotational symmetry [2, 3]. Similar structures have also been realized by growing bilayer graphene on top of the Ni [4, 5] or Cu surface [6, 7], and also by a transfer method [6].

The conventional moiré effective theory, which is based on the period of the moiré pattern arising from the interference between the lattice periods, cannot describe the electronic structures of such quasicrystals composed of incommensurate stack of atomic layers (hereafter "vdW-QCs") since the rotational symmetry of quasicrystals does not commute with translation. In our previous work, we developed a momentum-space tight-binding model which can describe the electronic structures of atomic layers stacked at any configuration without relying on the moiré periodicity [8]. This model enabled us to reveal the quasi-band dispersion and the emergence of the electronic states having the quasicrystalline order in the vdW-QC composed of two graphene layers stacked at 30° by fully respecting the rotational symmetry of quasicrystals as well as the translational symmetry of

constituent layers. While conventional quasicrystals can be viewed as *intrinsic quasicrystals* where all the atomic sites are intrinsically arranged in the quasiperiodic order, vdW-QCs are regarded as *extrinsic quasicrystals*, in that they are composed of a pair of perfect crystals having independent periodicities, and the quasiperiodic nature appears only in the perturbational coupling between the two subsystems. Thus, vdW-QCs provide a unique opportunity to design quasicrystalline states by using atomic layers with various symmetries and also to control the quasicrystalline interaction by controlling the interlayer interaction.

In this paper, we numerically investigate the electronic structures of vdW-QCs for every possible rotational symmetry in two-dimensional space. Since a periodic two-dimensional atomic layer can have 2-, 4-, 6-fold rotational symmetry, we can make only 8-fold [octagonal, Fig. 1(a)] or 12-fold [dodecagonal, Fig. 1(d)] vdW-QCs with two two-dimensional layers. This can be achieved by stacking two square lattices at 45° or by stacking two hexagonal lattices at 30° , respectively. We first find the resonant condition, which gives quasicrystalline order to the electronic states, in each system, and show that such resonant interaction emerges in this configuration if all the dominant interlayer interactions occur between the atomic orbitals that have the same magnetic quantum number. We calculate the quasi-band dispersion for various interlayer interaction strength, and identify the features which arise from the quasicrystalline order as opposed to those arising from the interaction common to any other θ in the spectrum of vdW-QCs. In addition, we show that some quasicrystalline states, which are usually obscured by additional weakly coupled states, are more prominent in vdW-QCs with strong interlayer interac-

* Corresponding author: pilkyung.moon@nyu.edu

tion. We also analyze the effects of lifting both interlayer and sublattice symmetry on the electronic structure, and discuss the mixing between the quasicrystalline states, which may influence the physical properties such as the optical selection rules.

The paper is organized as follows. In Sec. II, we present the atomic structures and tight-binding model for vdW-QCs, and introduce the dual tight-binding approach in the momentum space. And we reveal the resonant interaction which gives the quasicrystalline electronic states in vdW-QCs, and investigate the effects of atomic orbitals that have different symmetries. In Sec. III A and III B, we derive the minimal Hamiltonian and calculate the band dispersion and wave functions of octagonal and dodecagonal vdW-QCs, respectively. We also investigate the effects of various interlayer interaction strengths, the features arising from 2-wave mixing, and the effects of the lifting of interlayer and sublattice potential asymmetry. A brief conclusion is given in Sec. IV.

II. THEORETICAL METHODS

A. Atomic structure and Brillouin zones of quasicrystalline twisted bilayers

We define the atomic structure of the octagonal vdW-QCs by starting from two perfectly overlapping square lattices and rotating the layer 2 around the center of the square by $\theta = 45^\circ$ [Fig. 1(a)]. We set xy coordinates parallel to the layers and z axis perpendicular to them. The system belongs to the symmetry group D_{4d} , and it is invariant under an improper rotation $R(\pi/4)M_z$, where $R(\theta)$ is the rotation by an angle θ around z axis, and M_z is the mirror reflection with respect to xy plane. The primitive lattice vectors of layer 1 are taken as $\mathbf{a}_1 = a(1, 0)$ and $\mathbf{a}_2 = a(0, 1)$, where a is the lattice constant, and those of the layer 2 as $\tilde{\mathbf{a}}_i = R(\pi/4)\mathbf{a}_i$. In this paper, we model the square lattices by a minimal, one orbital model with one sublattice site. Then, the atomic positions are given by

$$\begin{aligned}\mathbf{R}_X &= n_1\mathbf{a}_1 + n_2\mathbf{a}_2 + \boldsymbol{\tau}_X & (\text{layer 1}), \\ \mathbf{R}_{\tilde{X}} &= \tilde{n}_1\tilde{\mathbf{a}}_1 + \tilde{n}_2\tilde{\mathbf{a}}_2 + \boldsymbol{\tau}_{\tilde{X}} & (\text{layer 2}),\end{aligned}\quad (1)$$

where n_i and \tilde{n}_i are integers, X (\tilde{X}) denotes the sublattice site (only one in this case) of layer 1 (layer 2) of which position in the unit cell is defined by $\boldsymbol{\tau}_X = (a/2, a/2)$ [$\boldsymbol{\tau}_{\tilde{X}} = R(\pi/4)\boldsymbol{\tau}_X + d\mathbf{e}_z$]. Here, d is the interlayer spacing between the two layers and \mathbf{e}_z is the unit vector normal to the layer. The reciprocal lattice vectors of layer 1 are given by $\mathbf{a}_1^* = (2\pi/a)(1, 0)$ and $\mathbf{a}_2^* = (2\pi/a)(0, 1)$, and layer 2 by $\tilde{\mathbf{a}}_i^* = R(\pi/4)\mathbf{a}_i^*$. The red and blue squares in Figs. 1(b) and (c) show the Brillouin zones of layer 1 and 2 in octagonal vdW-QCs, respectively.

Likewise, we define the atomic structure of the dodecagonal vdW-QCs by starting from two perfectly overlapping hexagonal lattices (i.e., AA-stacked bilayers) and

rotating the layer 2 around the center of the hexagon by $\theta = 30^\circ$ [Fig. 1(d)]. The system belongs to the symmetry group D_{6d} , and it is invariant under an improper rotation $R(\pi/6)M_z$. The primitive lattice vectors of layer 1 are taken as $\mathbf{a}_1 = a(1, 0)$ and $\mathbf{a}_2 = a(1/2, \sqrt{3}/2)$, where a is the lattice constant, and those of the layer 2 as $\tilde{\mathbf{a}}_i = R(\pi/6)\mathbf{a}_i$. The atomic positions are given by Eq. (1), where $X = A, B$ ($\tilde{X} = \tilde{A}, \tilde{B}$) denotes the sublattice site of layer 1 (2), and $\boldsymbol{\tau}_X$ and $\boldsymbol{\tau}_{\tilde{X}}$ are the sublattice positions in the unit cell, defined by $\boldsymbol{\tau}_A = -\boldsymbol{\tau}_1$, $\boldsymbol{\tau}_B = \boldsymbol{\tau}_1$, $\boldsymbol{\tau}_{\tilde{A}} = -R(\pi/6)\boldsymbol{\tau}_1 + d\mathbf{e}_z$, $\boldsymbol{\tau}_{\tilde{B}} = R(\pi/6)\boldsymbol{\tau}_1 + d\mathbf{e}_z$ with $\boldsymbol{\tau}_1 = (0, a/\sqrt{3})$, where d is the interlayer spacing between the two layers. The reciprocal lattice vectors of layer 1 are given by $\mathbf{a}_1^* = (2\pi/a)(1, -1/\sqrt{3})$ and $\mathbf{a}_2^* = (2\pi/a)(0, 2/\sqrt{3})$, and layer 2 by $\tilde{\mathbf{a}}_i^* = R(\pi/6)\mathbf{a}_i^*$. The red and blue hexagons in Fig. 1(e) and (f) show the Brillouin zones of layer 1 and 2 in dodecagonal vdW-QCs, respectively.

B. Tight-binding model for van der Waals bilayers

We model both systems by the tight-binding model with spherical harmonic orbitals of arbitrary atomic species. Although we use a single p_z orbital in this paper, just like the model of graphene and hexagonal boron nitride, but it can be any other orbital optimal for each system. We discuss the effects of using other kinds of orbitals in Sec. II E.

The Hamiltonian is spanned by the Bloch bases of each sublattice,

$$\begin{aligned}|\mathbf{k}, X\rangle &= \frac{1}{\sqrt{N}} \sum_{\mathbf{R}_X} e^{i\mathbf{k}\cdot\mathbf{R}_X} |\mathbf{R}_X\rangle \quad (\text{layer 1}), \\ |\tilde{\mathbf{k}}, \tilde{X}\rangle &= \frac{1}{\sqrt{N}} \sum_{\mathbf{R}_{\tilde{X}}} e^{i\tilde{\mathbf{k}}\cdot\mathbf{R}_{\tilde{X}}} |\mathbf{R}_{\tilde{X}}\rangle \quad (\text{layer 2}),\end{aligned}\quad (2)$$

where $|\mathbf{R}_X\rangle$ is the atomic orbital at the site \mathbf{R}_X , \mathbf{k} and $\tilde{\mathbf{k}}$ are the two-dimensional Bloch wave vectors and $N = S_{\text{tot}}/S$ is the number of the unit cells with an area S [$S = a^2$ for square lattices and $S = (\sqrt{3}/2)a^2$ for hexagonal lattices] in the total system area S_{tot} . We use a two-center Slater-Koster parametrization [9, 10] for the transfer integral between any two p_z orbitals,

$$-T(\mathbf{R}) = V_{pp\pi} \left[1 - \left(\frac{\mathbf{R} \cdot \mathbf{e}_z}{|\mathbf{R}|} \right)^2 \right] + V_{pp\sigma} \left(\frac{\mathbf{R} \cdot \mathbf{e}_z}{|\mathbf{R}|} \right)^2, \quad (3)$$

where \mathbf{R} is the relative vector between two atoms, and

$$\begin{aligned}V_{pp\pi} &= V_{pp\pi}^0 e^{-(|\mathbf{R}|-a)/\delta_1}, \\ V_{pp\sigma} &= V_{pp\sigma}^0 e^{-(|\mathbf{R}|-3a)/\delta_2},\end{aligned}\quad (4)$$

for square lattices and

$$\begin{aligned}V_{pp\pi} &= V_{pp\pi}^0 e^{-(|\mathbf{R}|-a/\sqrt{3})/\delta_1}, \\ V_{pp\sigma} &= V_{pp\sigma}^0 e^{-(|\mathbf{R}|-1.36a)/\delta_2},\end{aligned}\quad (5)$$

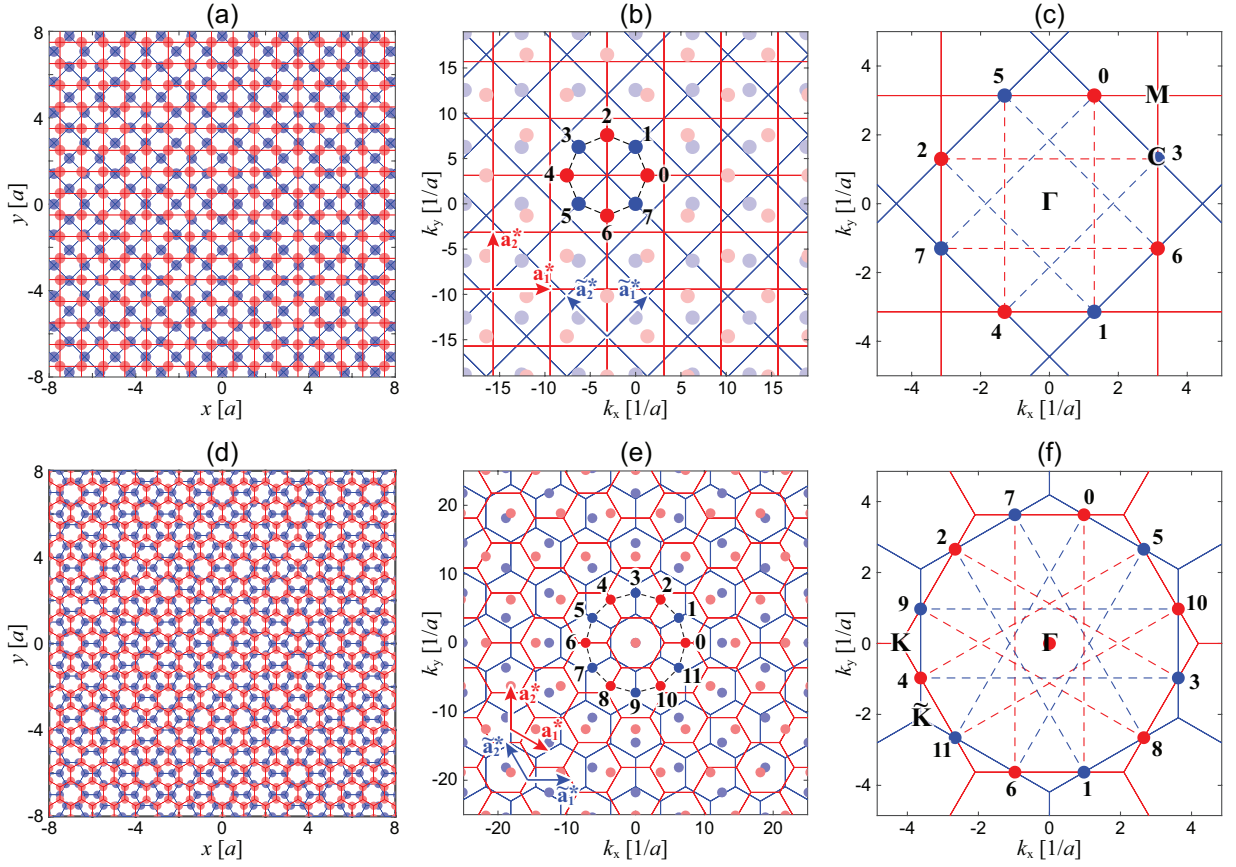


FIG. 1. (a) Real-space lattice structures of octagonal vdW-QCs. The red and blue squares represent the unit cells and the red and blue circles the atomic sites of layer 1 and 2, respectively. (b) Dual tight-binding lattice in the momentum space for octagonal vdW-QCs (see text). Red and blue squares show the extended Brillouin zones of layer 1 and 2, respectively. The number n represents the position of \mathbf{Q}_n ($n = 0, 1, 2, \dots, 7$), and the dashed lines indicate the connections in the 8-ring effective Hamiltonian. The red circles represent the wave numbers \mathbf{k} for layer 1, and blue ones represent the inverted wave numbers $\hat{\mathbf{k}} - \mathbf{k}$ for layer 2, where $\hat{\mathbf{k}}$ is taken as \mathbf{Q}_0 here. (c) The wave numbers \mathbf{C}_n ($n = 0, 1, 2, \dots, 7$) at the cross points between the first Brillouin zones of the two lattices, which are the original positions of \mathbf{k} (layer 1) and $\hat{\mathbf{k}}$ (layer 2) associated with \mathbf{Q}_n . The dashed lines indicate the connections in the 8-ring Hamiltonian as in (b). Due to the symmetry, these 8 wave numbers are all degenerate in energy. (d), (e), (f) Plots similar to (a), (b), (c) for dodecagonal vdW-QCs. Here, n for \mathbf{Q}_n and \mathbf{C}_n runs from 0 to 11, and $\hat{\mathbf{k}} = \mathbf{0}$.

for hexagonal lattices so that the first-nearest neighbor intralayer coupling becomes $V_{pp\pi}^0$. In both systems, we take $V_{pp\pi}^0 < 0$ and the decay length of the transfer integral as $\delta_1 = \delta_2 = 0.184a$ [11].

The total tight-binding Hamiltonian is expressed as

$$\mathcal{H} = \mathcal{H}_1 + \mathcal{H}_2 + \mathcal{U} + \mathcal{H}_V + \mathcal{H}_\Delta \quad (6)$$

where \mathcal{H}_1 and \mathcal{H}_2 are the Hamiltonian for the intrinsic square or hexagonal lattices of layer 1 and 2, respectively, \mathcal{U} is for the interlayer coupling, \mathcal{H}_V is for the interlayer potential asymmetry, and \mathcal{H}_Δ is for the sublattice potential asymmetry. The intralayer matrix elements of layer 1 are given by

$$\begin{aligned} & \langle \mathbf{k}', X' | \mathcal{H}_1 + \mathcal{H}_V + \mathcal{H}_\Delta | \mathbf{k}, X \rangle \\ & = [h_{X,X'}(\mathbf{k}) + \{V/2 + s_\Delta \Delta/2\} \delta_{X,X'}] \delta_{\mathbf{k}', \mathbf{k}}, \end{aligned} \quad (7)$$

where

$$h_{X,X'}(\mathbf{k}) = \sum_{\mathbf{L}} -T(\mathbf{L} + \boldsymbol{\tau}_{X'X}) e^{-i\mathbf{k} \cdot (\mathbf{L} + \boldsymbol{\tau}_{X'X})}, \quad (8)$$

and $\mathbf{L} = n_1 \mathbf{a}_1 + n_2 \mathbf{a}_2$, $\boldsymbol{\tau}_{X'X} = \boldsymbol{\tau}_{X'} - \boldsymbol{\tau}_X$, V is the magnitude of the interlayer potential asymmetry, s_Δ is $+1$ and -1 for $X = A$ and B , respectively, and Δ is the magnitude of the sublattice potential asymmetry. Note that the square lattices with the minimal, one orbital model considered in this work does not have the \mathcal{H}_Δ term as there is only one sublattice in this case. Similarly, the matrix for H_2 is given by replacing \mathbf{k} with $R(-\pi/4)\mathbf{k}$ in a square lattice and $R(-\pi/6)\mathbf{k}$ in a hexagonal lattice, $V/2$ with $-V/2$, and s_Δ by $+1$ and -1 for the sublattice \hat{A} and \hat{B} , respectively. For \mathcal{H}_1 and \mathcal{H}_2 , we consider only the nearest neighbor interactions in octagonal vdW-QCs to keep the symmetric and simple cosine bands, and all

interactions of $|\mathbf{R}|$ within $3a$ in dodecagonal vdW-QCs to make it consistent with previous works [2, 8, 12].

The interlayer matrix element between layer 1 and 2 is written as [13–15]

$$\begin{aligned} & \langle \tilde{\mathbf{k}}, \tilde{X} | \mathcal{U} | \mathbf{k}, X \rangle \\ &= - \sum_{\mathbf{G}, \tilde{\mathbf{G}}} t(\mathbf{k} + \mathbf{G}) e^{-i\mathbf{G} \cdot \boldsymbol{\tau}_X + i\tilde{\mathbf{G}} \cdot \boldsymbol{\tau}_{\tilde{X}}} \delta_{\mathbf{k} + \mathbf{G}, \tilde{\mathbf{k}} + \tilde{\mathbf{G}}}, \end{aligned} \quad (9)$$

where $\mathbf{G} = m_1 \mathbf{a}_1^* + m_2 \mathbf{a}_2^*$ and $\tilde{\mathbf{G}} = \tilde{m}_1 \tilde{\mathbf{a}}_1^* + \tilde{m}_2 \tilde{\mathbf{a}}_2^*$ ($m_1, m_2, \tilde{m}_1, \tilde{m}_2 \in \mathbb{Z}$) run over all the reciprocal points of layer 1 and 2, respectively. Here

$$t(\mathbf{q}) = \frac{1}{S} \int T(\mathbf{r} + z_{\tilde{X}X} \mathbf{e}_z) e^{-i\mathbf{q} \cdot \mathbf{r}} d\mathbf{r} \quad (10)$$

is the in-plane Fourier transform of the transfer integral, where $z_{\tilde{X}X} = (\boldsymbol{\tau}_{\tilde{X}} - \boldsymbol{\tau}_X) \cdot \mathbf{e}_z$. Note that both $T(\mathbf{R})$ and $t(\mathbf{q})$ between two p_z orbitals in the framework of a two-center Slater-Koster parametrization are isotropic along the in-plane direction, i.e., $T(\mathbf{R}) = T(|\mathbf{R}|)$ and $t(\mathbf{q}) = t(|\mathbf{q}|)$.

C. Dual tight-binding model in momentum space

In real-space, since quasicrystals do not have periodicity, we need infinitely many atomic orbital bases to solve Eq. (6). Although some conventional approximations with a finite number of bases, such as a periodic approximant or a finite-size model, can give an energy spectrum quite similar to the actual spectrum, the resulting wave functions lose their long-range quasicrystalline nature, and spurious states, such as the boundary states, can emerge. In addition, the use of the conventional theory on periodic moiré superlattices cannot be validated in vdW-QCs due to the absence of the moiré periodicity.

Instead, we can solve Eq. (6) rigorously by using a tight-binding model in momentum space, which is the dual counterpart of the original tight-binding Hamiltonian in the real space. Equation (9) shows that the interlayer interaction occurs between the states satisfying the generalized Umklapp scattering condition $\mathbf{k} + \mathbf{G} = \tilde{\mathbf{k}} + \tilde{\mathbf{G}}$. It is straightforward to show that the entire subspace spanned by $\mathcal{H}_1 + \mathcal{H}_2 + \mathcal{U}$ from a layer 1's Bloch state at $\hat{\mathbf{k}}$ is given by $\{|\mathbf{k}, X\rangle | \mathbf{k} = \hat{\mathbf{k}} + \tilde{\mathbf{G}}, \forall \tilde{\mathbf{G}}\}$ and $\{|\tilde{\mathbf{k}}, \tilde{X}\rangle | \tilde{\mathbf{k}} = \hat{\mathbf{k}} + \mathbf{G}, \forall \mathbf{G}\}$. According to Eq. (9), the interaction strength between $\mathbf{k} = \hat{\mathbf{k}} + \tilde{\mathbf{G}}$ and $\tilde{\mathbf{k}} = \hat{\mathbf{k}} + \mathbf{G}$ is given by $t(\mathbf{q})$ where $\mathbf{q} = \mathbf{k} + \mathbf{G} = \tilde{\mathbf{k}} + \tilde{\mathbf{G}} = \mathbf{k} - (\hat{\mathbf{k}} - \tilde{\mathbf{k}})$. Then, the interaction strength can be visualized by the diagram Figs. 1(b) and (e), where all the layer 2's wave points $\tilde{\mathbf{k}}$ are inverted with respect to $\hat{\mathbf{k}}$, i.e., $(\hat{\mathbf{k}} - \tilde{\mathbf{k}})$, and overlapped with the layer 1's wave points \mathbf{k} . In the map, the quantity $|\mathbf{q}| = |\mathbf{k} - (\hat{\mathbf{k}} - \tilde{\mathbf{k}})|$ is the geometrical distance between two points, and the interaction takes place only between the points located in close distance, since $t(\mathbf{q})$ decays in large \mathbf{q} . If the k points are viewed as

"sites", the whole system can be recognized as a tight-binding lattice in the momentum space, which is dual to the original Hamiltonian in the real space. This enables us to calculate the electronic structures of almost every possible stack of atomic layers without relying on moiré periodicity.

In this momentum-space tight-binding model, the hopping between different momentum space sites (the interlayer interaction \mathcal{U}) is an order of magnitude smaller than the potential landscape (the band energies of the monolayers). Thus, the eigenfunctions tend to be localized in momentum space in a similar manner to the Aubry-André model in one dimensional real-space lattice under incommensurate perturbation [16]. Therefore, in practical calculation, we only need a limited number of states around $\hat{\mathbf{k}}$ inside a certain cut-off circle k_c . The k_c should be greater than the typical localization length in momentum space, but need not be too large, since the wave points discarded outside k_c are properly accounted for by shifting $\hat{\mathbf{k}}$ within the first Brillouin zone. If we increase k_c , we will see more and more replicas of the identical quasi-energy band with different origins, because shifting $\hat{\mathbf{k}}$ actually corresponds to taking a different origin in the momentum space map of Figs. 1(b) and 1(e). The analysis on the validity of the momentum-space cut-off in Ref. [8] shows that most states in van der Waals bilayers are made up of 20 or less monolayer states. Thus, $k_c \approx 20/a$, which includes a few hundreds of monolayer states within, is sufficient in most practical calculation, and we can obtain the energy eigenvalues at $\hat{\mathbf{k}}$ by diagonalizing the Hamiltonian matrix within this finite set of bases.

D. Resonant states respecting the rotational symmetry of quasicrystals

The rotational symmetry of the quasicrystal as well as the translational symmetries of the constituent atomic layers [Eq. (9)] reveal the most dominant interaction, which comes from the resonance between degenerate states, in each vdW-QC. In octagonal vdW-QCs, we see that the eight symmetric points $\mathbf{Q}_n = [-\pi/a, \pi/a] + (a^*/\sqrt{2})[\cos(n\pi/4), \sin(n\pi/4)]$ ($n = 0, 1, 2, \dots, 7$) form a circular chain in the dual tight-binding lattice with $\hat{\mathbf{k}} = \mathbf{Q}_0$. The chain has a radius of $a^*/\sqrt{2} \equiv |\mathbf{a}_i^*|/\sqrt{2} = \sqrt{2}\pi/a$, and is indicated by the dashed ring in Fig. 1(b). Noting that the layer 2's wave points are inverted, these points are associated with layer 1's Bloch wave numbers $\mathbf{k} = \mathbf{Q}_n$ for even n 's and layer 2's $\tilde{\mathbf{k}} = \mathbf{Q}_0 - \mathbf{Q}_n$ for odd n 's. Figure 1(c) shows the original positions of \mathbf{k} (layer 1) and $\tilde{\mathbf{k}}$ (layer 2) associated with \mathbf{Q}_n in the first Brillouin zone, $\mathbf{C}_n = \sqrt{2}a^* \sin(\pi/8)[\cos(3\pi/8 + 5n\pi/4), \sin(3\pi/8 + 5n\pi/4)]$ ($n = 0, 1, 2, \dots, 7$). Each intrinsic square lattice has a single cosinusoidal band with a band maximum and minimum at M- and Γ -points of the Brillouin zone, respectively. Due to the symmetry, the Bloch states of the

intrinsic lattices at the eight points are all degenerate in energy, and therefore the interlayer coupling hybridizes them to make quasicrystalline resonant states. Here the coupling is only relevant between the neighboring sites of the ring, and it is given by $t_0 \equiv t(|\mathbf{C}_n|)$. The interaction to other neighboring states in the dual tight-binding lattice can be safely neglected since the interaction strength is much less than t_0 and the two states are not degenerate in most cases.

Likewise, in dodecagonal vdW-QCs, we see that the twelve symmetric points $\mathbf{Q}_n = a^*[\cos(n\pi/6), \sin(n\pi/6)]$ ($n = 0, 1, 2, \dots, 11$) form a circular chain in the dual tight-binding lattice with $\hat{\mathbf{k}} = \mathbf{0}$ and the radius is $a^* \equiv |\mathbf{a}_i^*| = 4\pi/(\sqrt{3}a)$ [dashed ring in Fig. 1(e)]. These points are associated with layer 1's Bloch wave numbers $\mathbf{k} = \mathbf{Q}_n$ for even n 's and layer 2's $\mathbf{k} = -\mathbf{Q}_n$ for odd n 's, and Fig. 1(f) shows the original positions of \mathbf{k} (layer 1) and \mathbf{k} (layer 2) associated with \mathbf{Q}_n in the first Brillouin zone, $\mathbf{C}_n = 2a^* \sin(\pi/12)[\cos(5\pi/12 + 7n\pi/6), \sin(5\pi/12 + 7n\pi/6)]$ ($n = 0, 1, 2, \dots, 11$). Again, the Bloch states of each intrinsic hexagonal lattice at the twelve points are all degenerate in energy and hybridized to form quasicrystalline resonant states by interlayer coupling with $t_0 \equiv t(|\mathbf{C}_n|)$.

It should be noted that these states are not the only set of states which show the resonant coupling in each system. As we shown in Appendix A, there are more sets of states, with different wave numbers, that show the resonant interaction respecting the rotational symmetry of the quasicrystals. However, the sets in Figs. 1(b) and (e) give the strongest interaction, i.e., largest energy separation between the quasicrystalline states, since these states form the rings with the shortest distance between neighboring states in the dual tight-binding lattices.

E. Quasicrystals from general atomic layers

The quasicrystalline resonant states emerge from the degeneracy of the constituent monolayer states and the equivalence of the interlayer coupling strength at all of the symmetric points \mathbf{C}_n in the Brillouin zone. The former is always guaranteed by the symmetry of atomic layers as long as we use two identical atomic layers. The latter, however, depends on the atomic orbitals involved. In Sec. II B, we described the Hamiltonian of van der Waals bilayers of which electronic structures are described mainly by a single p_z orbital at each atomic site. However, we can obtain the quasicrystalline configuration from any kind of atomic layers with a square or hexagonal lattice symmetry, some of which are better described by, one or more, other types of orbital.

It is straightforward to show that the transfer integral and interlayer coupling strength between the atomic orbitals with spherical harmonics Y_l^m and $Y_l^{m'}$, where l is the angular momentum quantum numbers and m stands for the magnetic quantum number of atomic or-

bitals (only in this subsection), are

$$\begin{aligned} -T(\mathbf{R}) &= F(|\mathbf{R}|)e^{i(m'-m)\phi_{\mathbf{R}}}, \\ -t(\mathbf{q}) &= f(|\mathbf{q}|)e^{i(m'-m)(\phi_{\mathbf{q}}+\pi/2)}, \end{aligned} \quad (11)$$

where $\phi_{\mathbf{R}}$ and $\phi_{\mathbf{q}}$ are the azimuthal angle of \mathbf{R} and \mathbf{q} measured from x axis to counterclockwise direction, respectively, and $F(|\mathbf{R}|)$ and $f(|\mathbf{q}|)$ are real functions that do not depend on $\phi_{\mathbf{R}}$ and $\phi_{\mathbf{q}}$, respectively. Equation (11) shows that $t(\mathbf{q})$ between the atomic orbitals with the same m is isotropic, while that between different m is not; it is instead $|m-m'|$ -fold rotational symmetric and works as a potential with $1/|m-m'|$ period of the ring in the dual tight-binding lattice. Thus, replacing the p_z orbital in Sec. II B with another spherical harmonic orbital changes only the magnitude of quasicrystalline interaction and does not influence the topology of the quasicrystalline bands and the symmetry of the wave functions. Meanwhile, vdW-QCs composed of atomic layers with multiple atomic orbitals exhibit the resonant interaction respecting the rotational symmetry of the quasicrystals if all the dominant interlayer interactions occur between the atomic orbitals having the same m ; otherwise, they exhibit the resonant interaction with a lower rotational symmetry.

In transition metal dichalcogenides (TMDC) monolayers, both the first conduction band and valence band are predominantly from the d_{z^2} and $d_{xy} + d_{x^2-y^2}$ (i.e., Y_2^0 and $Y_2^{\pm 1}$) orbitals of the metal atoms [17–19]. In TMDC bilayers, however, the interaction between the d -orbitals in different layers is negligible since the metal atoms in different TMDC layers are largely separated. Instead, the dominant interlayer interaction comes from the orbital hybridization between the p_z (Y_1^0) orbitals of the adjacent chalcogen layers (of an order of sub-eV in MoS₂ bilayer) [19–21], and the next strongest interaction (of an order of tens of meV in MoS₂ 2H bilayer) comes from the coupling between d_{z^2} and p_z [19]. Thus, we need all of these orbitals, Y_2^0 , $Y_2^{\pm 1}$, Y_1^0 , to describe the electronic structures of the quasicrystals composed of TMDC layers. As Eq. (11) shows, the strongest (between Y_1^0) and the next strongest (between Y_2^0 and Y_1^0) interlayer interaction exhibit isotropic $t(\mathbf{q})$. Although $t(\mathbf{q})$ between $Y_2^{\pm 1}$ and Y_1^0 is anisotropic, the interaction strength is at least 1 to 2 order weaker than the strongest interaction since the spatial extension of $Y_2^{\pm 1}$ to the interlayer region is less than that of Y_2^0 . Thus, most TMDC vdW-QCs will also show the resonant states respecting the rotational symmetry of the quasicrystals.

III. RESULTS AND DISCUSSION

Below, we first investigate the electronic structures of a vdW-QC in the absence of the interlayer and sublattice potential asymmetry by using a dual-tight binding method with $t(\mathbf{q})$ obtained at a specific combination of $(V_{pp\sigma}^0, d)$. We investigate the electronic structures of

vdW-QCs predominantly described by a single spherical harmonic orbital of any type.

Then we investigate the change in the band structure with respect to changes of constituent materials or, equivalently, to changes in the interaction strength, which can be tuned by varying $t(\mathbf{q})$. If two different vdW-QCs have the same sublattice configuration, the interactions [Eq. (9)] in the two systems will have the same phase and differ only in the magnitude of the interaction $t(\mathbf{q})$. Thus, the quasi-band dispersion near \mathbf{C}_n is mainly governed by the magnitude of $t_0 = t(\mathbf{C}_n)$, together with the dispersion of the monolayer states, and we can investigate the electronic structures of various vdW-QCs by simply scaling t_0 . In addition, scaling t_0 also shows the effects of tuning the interlayer interaction in a given vdW-QC with the interlayer distance d , e.g., by applying an external pressure or intercalation, since the magnitude of the interlayer transfer integral Eq. (3) exponentially decays with d [22].

Then finally, we study the effects of breaking the interlayer or sublattice symmetry.

A. Octagonal quasicrystal

1. Hamiltonian

In octagonal vdW-QCs, the strongest quasicrystalline resonant interaction occurs at $\hat{\mathbf{k}} = \mathbf{Q}_0$. By replacing $\hat{\mathbf{k}}$ with $\mathbf{Q}_0 + \mathbf{k}_0$, we can express the Hamiltonian

$$\mathcal{H} = \mathcal{H}_{\text{ring}} + \mathcal{H}_V, \quad (12)$$

in the vicinity of $\mathbf{k}_0 = \mathbf{0}$, in the bases of $(|\mathbf{k}^{(0)}\rangle, |\mathbf{k}^{(1)}\rangle, \dots, |\mathbf{k}^{(7)}\rangle)$, where $|\mathbf{k}^{(n)}\rangle$ is $|\mathbf{k}_0 + \mathbf{C}_n, X\rangle$ for even n (layer 1) and $|\mathbf{k}_0 + \mathbf{C}_n, \tilde{X}\rangle$ for odd n (layer 2). Here,

$$\mathcal{H}_{\text{ring}}(\mathbf{k}_0) = \begin{pmatrix} H^{(0)} & -t_0 & & & -t_0 \\ -t_0 & H^{(1)} & -t_0 & & \\ & -t_0 & H^{(2)} & -t_0 & \\ & & \ddots & \ddots & \ddots \\ & & & -t_0 & H^{(6)} & -t_0 \\ -t_0 & & & & -t_0 & H^{(7)} \end{pmatrix}, \quad (13)$$

is the Hamiltonian matrix of the resonant ring in the absence of interlayer potential asymmetry, where $H^{(n)}(\mathbf{k}_0) = h_{X,X}[R(-5n\pi/4)\mathbf{k}_0 + \mathbf{C}_0]$, and we neglect the \mathbf{k}_0 dependence of the interlayer matrix element $t(\mathbf{q})$. The diagonal elements $H^{(n)}$ represent monolayer's Hamiltonian at $\mathbf{k} = \mathbf{k}_0 + \mathbf{C}_n$ for even n and $\tilde{\mathbf{k}} = \mathbf{k}_0 + \mathbf{C}_n$ for odd n . Note that $h_{X,X}$ in $H^{(n)}$ is same for any n , and the dependence of the diagonal elements on n solely comes from $R(-5n\pi/4)\mathbf{k}_0$ in the argument of $h_{X,X}$. Consequently, the ring Hamiltonian $\mathcal{H}_{\text{ring}}$ is obviously symmetric under rotation by a single span of the ring (i.e., moving \mathbf{C}_n to \mathbf{C}_{n+1}), which actually corresponds to the operation

$[R(\pi/4)M_z]^5$ (225° rotation and swapping layer 1 and 2) in the original system. In addition, $\mathcal{H}_{\text{ring}}$ has a particle-hole symmetry with respect to the energy $E = h_0$, where $h_0 \equiv h_{X,X}(\mathbf{C}_0) \approx -2V_{pp\pi}^0(\cos\sqrt{2}\pi + 1)$, up to the first order to \mathbf{k}_0 (Appendix B).

\mathcal{H}_V is the Hamiltonian representing the interlayer potential asymmetry,

$$\mathcal{H}_V = \frac{V}{2} \begin{pmatrix} \sigma_z & & & \\ & \sigma_z & & \\ & & \sigma_z & \\ & & & \sigma_z \end{pmatrix}, \quad (14)$$

where V (≥ 0) represents the difference in the electrostatic energies between the two layers, and σ_z is the Pauli matrix. With \mathcal{H}_V , the Hamiltonian \mathcal{H} , which was originally in the form of one-dimensional monatomic chain in the dual-tight binding lattice, becomes that of diatomic chain with alternating on-site potential.

2. Band structures and wave functions

Figure 2(a) shows the band structures of the octagonal vdW-QCs near \mathbf{C}_n , in the absence of interlayer potential asymmetry (i.e., $V = 0$), plotted as a function of \mathbf{k}_0 , and Fig. 2(b) shows its closer view near $\mathbf{k}_0 = \mathbf{0}$. We choose $(V_{pp\sigma}^0, d) = (-0.142V_{pp\pi}^0, 2.97a)$, which gives an interaction strength between the neighboring sites of the circular chain in the dual-tight binding lattice of $t_0 = 0.0296V_{pp\pi}^0$. The eight parabolic bands are arranged on a circle with a radius $\Delta k = (2 - \sqrt{2})\pi/a$ by the Umklapp scattering [Eq. (9)], and they are strongly hybridized near $\mathbf{k}_0 = \mathbf{0}$. As a result, the originally degenerate eight states of the square lattices split into different energies and exhibit characteristic dispersion, including parabolic band-bottoms and a frilled band edge, which is flat up to the first order in \mathbf{k}_0 .

At $\mathbf{k}_0 = \mathbf{0}$, $\mathcal{H}_{\text{ring}}$ can be analytically diagonalized to obtain a set of energies

$$E_m = h_0 - 2t_0 \cos q_m, \quad (15)$$

which have the energy span of $4t_0$, where $q_m = (5\pi/4)m$ with $m = 0, \pm 1, \pm 2, \pm 3, 4$ the wave number along the chain. Each element of the eigenvectors $\mathbf{v}_m = (\mu_m^{-3}, \mu_m^{-2}, \mu_m^{-1}, \dots, \mu_m^4)/\sqrt{8}$ ($\mu_m = e^{iq_m}$) is the coefficient to the Bloch bases $|\mathbf{k}^{(0)}\rangle, |\mathbf{k}^{(1)}\rangle, \dots, |\mathbf{k}^{(7)}\rangle$. Here the states with $m = \pm s$ ($s = 1, 2, 3$) form twofold doublets, and belong to two-dimensional E_s irreducible representation of D_{4d} point group, while the $m = 0$ and 4 are non-degenerate, and belong to A_1 and B_2 , respectively. If we disregard the z -position difference, the index m can be regarded as quantized angular momentum. The fact that there are 8 unique values for m as well as the fact that the eigenvalue of $R(\pi/4)M_z$ is given by $e^{i\pi m/4}$ are the evidence that the quasicrystalline electronic states respect an 8-fold rotational symmetry.

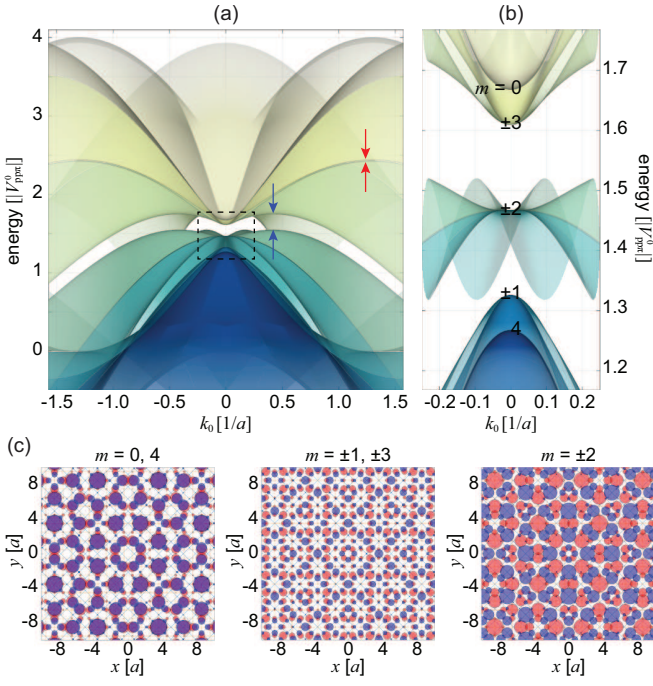


FIG. 2. (a) Electronic structure of octagonal vdW-QCs calculated by the 8-ring effective model. The blue and red arrows show the band opening by the interlayer and intralayer 2-wave mixing, respectively (see Sec. III A 3). (b) Detailed band structures near $\mathbf{k} = \mathbf{C}_n$ [the region encircled by the black dashed rectangle in (a)] with index m indicating the quantized angular momentum of the 8-fold rotational symmetry. (c) LDOS at $\mathbf{k} = \mathbf{C}_n$ characterized by m , where the area of the circle is proportional to the squared wave amplitude, and red and blue circles represent the states in the upper and the lower layers, respectively.

The 8-wave resonant coupling also gives rise to a characteristic pattern in the wave function. Figure 2(c) shows the wave functions at $\mathbf{k}_0 = \mathbf{0}$ where the hybridization is the most prominent. We can see that the wave amplitude is distributed on a limited number of sites in a 8-fold rotationally symmetric pattern.

3. The effect of the interlayer interaction and 8- and 2-wave mixing

As discussed in the beginning of this section, we can calculate the quasicrystalline states of various octagonal vdW-QCs, which are either composed of other materials or different interlayer distance d , by simply scaling the magnitude of the interlayer interaction $t(\mathbf{q})$. Figure 3(a) shows the band structures of an octagonal vdW-QC with $t(\mathbf{q})$ 2 times larger than that in Fig. 2. Although the interaction strength varies with \mathbf{q} , hereafter we label each system with $t(\mathbf{q})$ at \mathbf{q} showing the strongest quasicrystalline interaction, $t_0 [= t(\mathbf{C}_n)]$. The stronger t_0 makes the 8-waves interact over a much wider area in

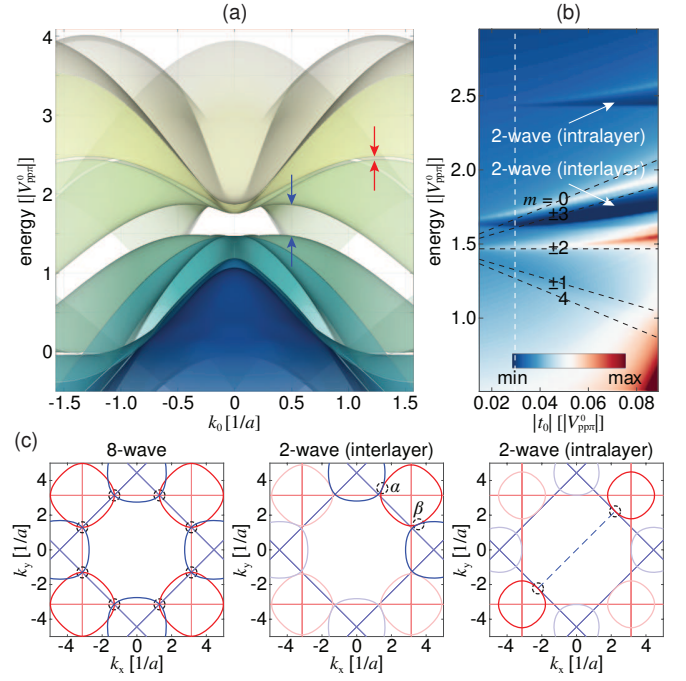


FIG. 3. (a) Electronic structures of octagonal vdW-QCs with the interlayer interaction $|t_0|$ 2 times larger than that in Fig. 2. The blue and red arrows show the band opening by the interlayer and intralayer 2-wave mixing, respectively. (b) Density map of DOS calculated by using 32-waves and band edges of the quasicrystalline states [black dashed lines, Eq. (15)] with various t_0 . The white dashed line corresponds to the DOS for the system considered in Fig. 2. The white arrows show the pseudogaps opened by the interlayer and intralayer 2-wave interaction. (c) Three representative interactions residing in octagonal vdW-QCs; quasicrystalline interaction by 8-wave mixing (left), interlayer 2-wave mixing (middle), and intralayer 2-wave mixing (right). The red and blue contours show the Fermi surfaces of layer 1 and 2, respectively, the black dashed circles show the wave numbers where the interaction occurs, and the blue dashed line shows the reciprocal lattice vector of layer 2 which mediates the interaction between the states in layer 1.

the Brillouin zone, and the energy spacing between the quasicrystalline states larger. Accordingly, the $m = \pm 2$ states become flatter and the band curvature of the other states increases.

The density map in Fig. 3(b) shows the density of states (DOS) of octagonal vdW-QCs with various t_0 , with the white dashed line corresponding to the DOS for the system considered in Fig. 2. The large DOS observed at lower energies in the systems with a large $|t_0|$ reflects the flat bands arising from the 2-wave mixing at Γ . While the eight Bloch states centered at \mathbf{C}_n are sufficient to fully describe the resonant interaction governing the quasicrystalline states, some minor interactions at other wave vectors are not captured by these bases. Thus, we used more (32 waves) bases to calculate the DOS in wider energy range. We also plot the band edges of the quasicrystalline

states [Eq. (15)] by black dashed lines. As $|t_0|$ increases, the energy spacing between the edges increases and the height of the DOS peaks also grows rapidly. It should be noted that some band edges (e.g., $m = \pm 2$) lead to a series of characteristic spiky peaks in DOS and dips (pseudogaps) in between, while other edges are buried in the DOS of weakly coupled states. Thus, quasicrystalline features, such as local density of states (LDOS) with 8-fold rotational symmetry and relevant physical properties, are most prominent at the energies where the band edges coincide with the spiky peaks in DOS. As changing t_0 does not break the symmetry of the Hamiltonian, it neither changes the symmetry nor the degeneracy of quasicrystalline states.

In addition to the features from the quasicrystalline 8-wave mixing, Fig. 3(b) shows the peaks and pseudogaps associated with other kinds of interaction. We plot the wave numbers associated with these interactions in Fig. 3(c), together with the Fermi surfaces. The middle panel shows the 2-wave mixing between the states in different layers [12], which occurs when the Fermi surfaces of the two layers meet, while the right panel shows the 2-wave mixing between the states in the same layer assisted by the potential of the opposite layer [5, 22]. Blue and red arrows in Figs. 2(a) and 3(a) show the band opening by the interlayer and intralayer 2-wave mixing, respectively, whose size also increases with $|t_0|$. The interlayer interaction strength $t(\mathbf{q})$ involved in the interlayer and intralayer 2-wave mixing is 0.472 and 1.49 times the interaction strength t_0 for the 8-wave interaction. However, the intralayer mixing exhibits a band opening smaller than the interlayer mixing partly due to the two successive interlayer interaction and partly due to the energy difference between the states in opposite layers. At $t_0 \rightarrow 0$ limit, the 8-wave, interlayer 2-wave, intralayer 2-wave mixing emerge at the energies $E = \cos \sqrt{2}\pi + 1 (\approx 1.47)$, $-2 \cos \frac{\sqrt{2}+1}{2}\pi (\approx 1.59)$, $-4 \cos(\pi/\sqrt{2}) (\approx 2.42)$ in unit of $|V_{pp\pi}^0|$. It should be noted that the states and band opening arising from these three mixing are continuously connected to each other in the Brillouin zone [Figs. 3(a) and (c)]. Unlike the quasicrystalline 8-wave interaction, both the 2-wave mixing processes can occur in bilayer square lattices stacked at any rotation angle θ , i.e., at usual moiré superlattices. However, it is straightforward to show that α and β in Fig. 3(c), which is typically known as a *moiré interaction*, occur at different energies [12] in the systems with θ other than 45° .

4. Effects of interlayer potential asymmetry

Figure 4(a) shows the band dispersion near \mathbf{C}_n of octagonal vdW-QCs under three different interlayer asymmetric potential, $V = 0, 0.1, 0.2$ in unit of $|V_{pp\pi}^0|$. Since Eq. (12) satisfies $\Sigma'^{-1}(\mathcal{H} - h_0\mathbb{I})\Sigma' = -(\mathcal{H} - h_0\mathbb{I})$ at $\mathbf{k}_0 = \mathbf{0}$ for $\Sigma' = \text{diag}(i\sigma_y, i\sigma_y, i\sigma_y, i\sigma_y)$ and \mathbb{I} is an 8×8 unit matrix, regardless of the presence of the interlayer potential asymmetry, \mathcal{H} has a particle-hole symmetry with respect

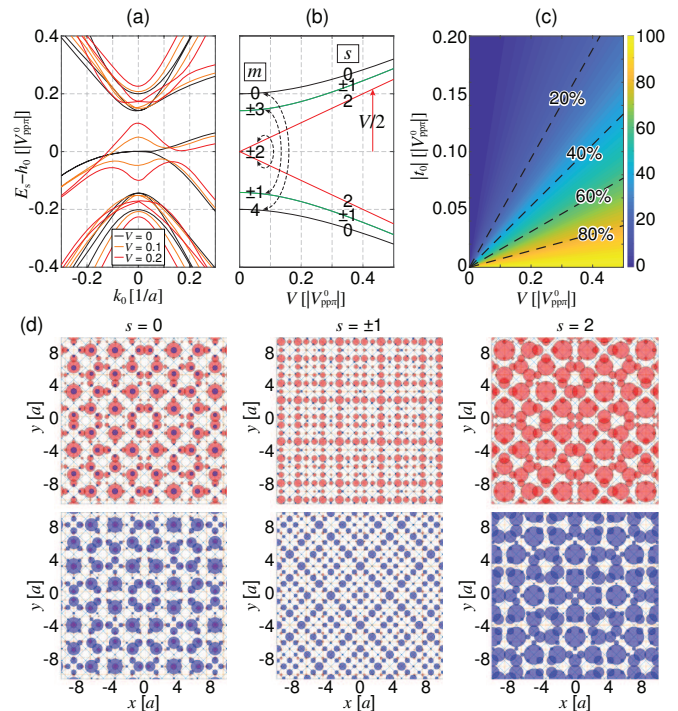


FIG. 4. (a) Band dispersion near \mathbf{C}_n of octagonal vdW-QCs under three different interlayer potential asymmetry, $V = 0, 0.1 |V_{pp\pi}^0|, 0.2 |V_{pp\pi}^0|$. (b) Band edges at \mathbf{C}_n with various V . Indices m and s show the angular momentum of the pristine quasicrystalline states with 8-fold rotational symmetry and that of 4-fold rotational symmetry under interlayer potential asymmetry. Dashed arrows show the interaction between the constituent quasicrystalline states by \mathcal{H}_V . (c) Degree of mixing (in percentage) between the constituent states in $\Psi_{s=\pm 1}$ (see text) with respect to the interlayer interaction strength $|t_0|$ and interlayer potential asymmetry V . (d) Plots similar to Fig. 2(c) for $V \neq 0$. The top and bottom panels show the LDOS of the upper and lower bands, respectively.

to the energy $E = h_0$. As V increases, however, the states with $m = \pm 2$ at $\mathbf{k}_0 = \mathbf{0}$ lose the degeneracy, and all the band edges move away from $E_{m=\pm 2} (= h_0)$.

We can obtain further insight on the effects of the interlayer potential asymmetry from the analytic expression of the energies at $\mathbf{k}_0 = \mathbf{0}$. The interlayer potential asymmetry couples the eigenstates of $\mathcal{H}_{\text{ring}}(\mathbf{k}_0 = \mathbf{0})$ that have angular momenta that differ by ± 4 ,

$$\langle \mathbf{v}_{m'} | \mathcal{H}_V | \mathbf{v}_m \rangle = \begin{cases} -V/2 & (m - m' \equiv 4 \pmod{8}), \\ 0 & (\text{otherwise}), \end{cases} \quad (16)$$

since the diagonal elements of \mathcal{H}_V work as a staggered potential with $1/4$ period of the ring in the dual tight-binding lattice. Thus, the Hamiltonian matrix in the bases of the quasicrystalline states is reduced to four 2×2 matrices

$$\tilde{\mathcal{H}}_{m,m'} = \begin{pmatrix} E_m & -V/2 \\ -V/2 & E_{m'} \end{pmatrix}, \quad (17)$$

for $(m, m') = (0, 4), (1, -3), (2, -2), (3, -1)$. As the quasicrystalline states, \mathbf{v}_m , originate from the resonant interaction between the degenerate states $|\mathbf{k}^{(n)}\rangle$ in the two layers, the interlayer potential asymmetry breaks the 8-fold rotational symmetry of the states by lifting the degeneracy of $|\mathbf{k}^{(n)}\rangle$. This reduces the allowed angular quantum numbers to $s (= 0, \pm 1, 2) \equiv m \equiv m' \pmod{4}$, which indicates a 4-fold rotational symmetry. We obtain the following energies and wave functions

$$\begin{aligned} E_s &= h_0 \pm \sqrt{4t_0^2 \cos^2(5\pi s/4) + V^2/4}, \\ \Psi_s &= c_m \mathbf{v}_m + c_{m'} \mathbf{v}_{m'}, \end{aligned} \quad (18)$$

where $(c_m, c_{m'})$ is $(\sin(\phi/2), -\cos(\phi/2))$ for the upper band and $(\cos(\phi/2), \sin(\phi/2))$ for the lower band with $\phi = \tan^{-1}(V/(4t_0 \cos q_m))$, and plot E_s against V in Fig. 4(b). The states with $s = 1$ and $s = -1$ are always degenerate due to the $\mathbf{v}_m^* = \mathbf{v}_{-m}$ symmetry of the wave functions. At small V , the interlayer interaction $|t_0|$ suppresses the energy shift of $s = 0, \pm 1$ states [Eq. (18)], in a similar manner to the way the interaction suppresses the Dirac point shift in twisted bilayer graphene with a small twist angle [23]. On the other hand, the two states with $s = 2$ ($m = \pm 2$) are composed of two degenerate quasicrystalline states, $m = 2$ and $m = -2$. Thus, their band edges shift as much as the applied bias in opposite directions and are not affected by the interlayer interaction t_0 as can be clearly seen from Eq. (17). As V increases, the overall energy span of these resonant states increases, while the energy spacing between the adjacent states decreases.

The dashed arrows in Fig. 4(b) show the interaction between quasicrystalline states between \mathbf{v}_m and $\mathbf{v}_{m'}$ by \mathcal{H}_V , and Fig. 4(c) shows the degree of mixing in $\Psi_{s=\pm 1}$, which we defined as $(1 - ||c_m|^2 - |c_{m'}|^2|) \times 100$ [%]. Systems with $|t_0| < V$ exhibit stronger mixing, which will influence the transition behavior, such as the optical selection rule, in vdW-QCs. The states with $s = 0$ exhibit a similar, but slightly weaker, mixing owing to the larger energy difference between E_m and $E_{m'}$ in $\Psi_{s=0}$. However, the states with $s = 2$ are special in that the constituent states \mathbf{v}_2 and \mathbf{v}_{-2} are always fully mixed, i.e., $c_{m'} = -c_m$ for the upper band and $c_{m'} = c_m$ for the lower band, regardless of the values of t_0 and V . Again, this is due to the degeneracy between the constituent states $m = 2$ and $m' = -2$.

We plot the LDOS of the upper and lower bands with $s = 0, \pm 1, 2$ at $V = 0.2 |V_{pp\pi}^0|$ in the top and bottom panels in Fig. 4(d), respectively. Due to the interlayer potential asymmetry, the wave functions Ψ_s are more or less spatially polarized to either layer. And the stronger the mixing, the more the wave functions are layer polarized; for example, $\Psi_{s=\pm 1}$ exhibit more polarization than $\Psi_{s=0}$. This is because

$$\Psi_s = \frac{1}{2}(c_m - c_{m'})(\mathbf{v}_m - \mathbf{v}_{m'}) + \frac{1}{2}(c_m + c_{m'})(\mathbf{v}_m + \mathbf{v}_{m'}), \quad (19)$$

where $(c_m, c_{m'}) \in \mathbb{R}$, and $\mathbf{v}_m - \mathbf{v}_{m'}$ and $\mathbf{v}_m + \mathbf{v}_{m'}$ are perfectly polarized to layer 1 and 2, respectively, since $\mu_{m'} = -\mu_m$. Thus, as the mixing becomes stronger, the upper bands ($c_{m'} \approx -c_m$) consist mostly of $|\mathbf{k}^{(n)}\rangle$ with even n (i.e., layer 1) while the lower bands ($c_{m'} \approx c_m$) consist mostly of $|\mathbf{k}^{(n)}\rangle$ with odd n (i.e., layer 2). Again, the states with $s = 2$ are special in that their wave functions $\Psi_{s=2}$ are perfectly polarized to either layer regardless of the values of t_0 and V because the constituent states \mathbf{v}_2 and \mathbf{v}_{-2} are always fully mixed. This is similar to the case of an one-dimensional diatomic chain whose sublattices stop completely at the acoustic and optical modes.

\mathbf{C}_n in Fig. 1(c), the wave vectors where quasicrystalline interaction occurs, remain the same since the interlayer potential asymmetry does not change the Umklapp scattering paths. Thus, the LDOS profile of each layer-polarized state, which is associated with \mathbf{C}_n for even n (layer 1) or \mathbf{C}_n for odd n (layer 2), is exactly consistent with the profile of each layer in the absence of the potential asymmetry [Fig. 2(c)]. Therefore, we can switch between the quasicrystalline states and their layer components by applying an electric field.

B. Dodecagonal quasicrystal

1. Hamiltonian

In dodecagonal vdW-QCs, the strongest quasicrystalline resonant interaction occurs at $\hat{\mathbf{k}} = \mathbf{0}$. Thus, by replacing $\hat{\mathbf{k}}$ with \mathbf{k}_0 , we can express the Hamiltonian of the resonant ring $\mathcal{H}_{\text{ring}}$ in the absence of the interlayer and sublattice potential asymmetry by a 24×24 matrix

$$\mathcal{H}_{\text{ring}}(\mathbf{k}_0) = \begin{pmatrix} H^{(0)} & W^\dagger & & & & W \\ W & H^{(1)} & W^\dagger & & & \\ & W & H^{(2)} & W^\dagger & & \\ & & \ddots & \ddots & \ddots & \\ & & & W & H^{(10)} & W^\dagger \\ W^\dagger & & & & W & H^{(11)} \end{pmatrix}, \quad (20)$$

$$H^{(n)}(\mathbf{k}_0) = \begin{pmatrix} h_{AA}^{(n)} & h_{AB}^{(n)} \\ h_{BA}^{(n)} & h_{BB}^{(n)} \end{pmatrix}, \quad W = -t_0 \begin{pmatrix} \omega & 1 \\ 1 & \omega^* \end{pmatrix}, \quad (21)$$

in the bases of $(|\mathbf{k}^{(0)}\rangle, |\tilde{\mathbf{k}}^{(1)}\rangle, |\mathbf{k}^{(2)}\rangle, |\tilde{\mathbf{k}}^{(3)}\rangle, \dots, |\mathbf{k}^{(11)}\rangle)$. Here, $\mathbf{k}^{(n)} = \mathbf{k}_0 + \mathbf{Q}_n$ for even n (layer 1) and $\tilde{\mathbf{k}}^{(n)} = \mathbf{k}_0 - \mathbf{Q}_n$ for odd n (layer 2), where $|\mathbf{k}^{(n)}\rangle$ and $|\tilde{\mathbf{k}}^{(n)}\rangle$ are $(|\mathbf{k}^{(n)}, X\rangle, |\mathbf{k}^{(n)}, X'\rangle)$ and $(|\tilde{\mathbf{k}}^{(n)}, \tilde{X}\rangle, |\tilde{\mathbf{k}}^{(n)}, \tilde{X}'\rangle)$ with the sublattices X and X' are arranged in the order of (A, B) or (\tilde{A}, \tilde{B}) for $n \equiv 0, 3$ modulo 4, and (B, A) or (\tilde{B}, \tilde{A}) for $n \equiv 1, 2$. And $h_{X'X}^{(n)}(\mathbf{k}_0) = h_{X'X}[R(-7n\pi/6)\mathbf{k}_0 + \mathbf{Q}_0]$, $\omega = e^{2\pi i/3}$, and we neglect the \mathbf{k}_0 dependence of the interlayer matrix element $t(\mathbf{q})$.

In the given bases order, the Hamiltonian representing

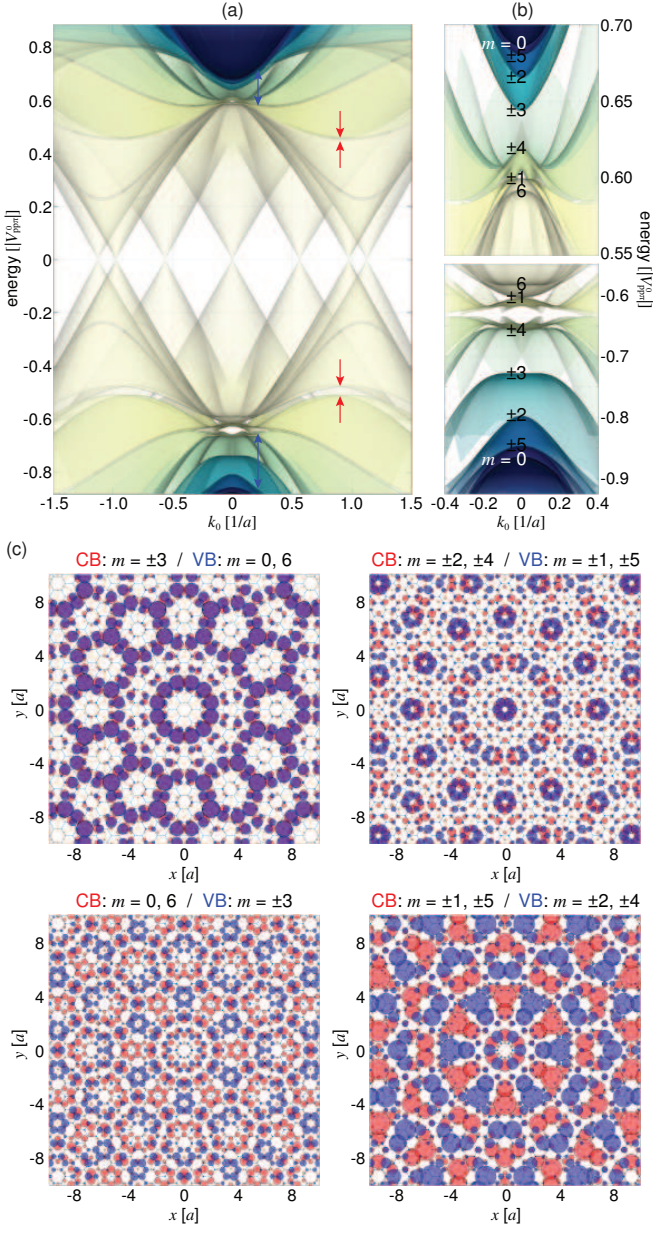


FIG. 5. Plots similar to Fig. 2 for dodecagonal vdW-QCs calculated by the 12-ring effective model. The blue and red arrows in (a) show the band opening by the interlayer and intralayer 2-wave mixing, respectively. The top and bottom panels in (b) show the quasicrystalline states in the conduction band and valence band, respectively.

the interlayer and sublattice potential asymmetry are expressed by

$$\mathcal{H}_V = \frac{V}{2} \text{diag}(\mathbb{I}, -\mathbb{I}, \mathbb{I}, -\mathbb{I}, \mathbb{I}, -\mathbb{I}, \mathbb{I}, -\mathbb{I}, \mathbb{I}, -\mathbb{I}, \mathbb{I}, -\mathbb{I}), \quad (22)$$

and

$$\mathcal{H}_\Delta = \frac{\Delta}{2} \text{diag}(\sigma_z, -\sigma_z, -\sigma_z, \sigma_z, \sigma_z, -\sigma_z, -\sigma_z, \sigma_z, \sigma_z, -\sigma_z, -\sigma_z, \sigma_z), \quad (23)$$

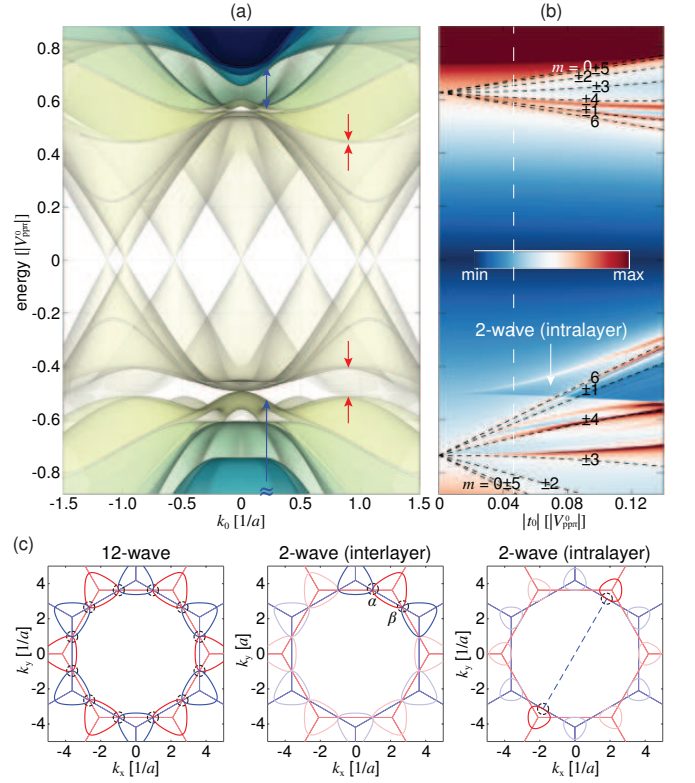


FIG. 6. (a) Electronic structures of dodecagonal vdW-QCs with the interlayer interaction $|t_0|$ 2 times larger than that in Fig. 5. The blue and red arrows show the band opening by the interlayer and intralayer 2-wave mixing, respectively. (b) Density map of DOS calculated by using 182-waves and band edges of the quasicrystalline states [black dashed lines, Eq. (25)] with various t_0 . The white dashed line corresponds to the DOS for the system considered in Fig. 5. (c) Plots similar to Fig. 3(c) in dodecagonal vdW-QCs.

respectively, where V represents the difference in the electrostatic energies between the two layers, Δ is the difference between the on-site potentials between two sublattices, and \mathbb{I} is a 2×2 unit matrix. Then, the Hamiltonian of general dodecagonal vdW-QCs is given by

$$\mathcal{H} = \mathcal{H}_{\text{ring}} + \mathcal{H}_V + \mathcal{H}_\Delta. \quad (24)$$

2. Band structures and wave functions

We plot the band structures near \mathbf{C}_n of the dodecagonal vdW-QCs with $(V_{pp\sigma}^0, d) = (-0.142 V_{pp\pi}^0, 1.36a)$ [24] and $V = 0$, $\Delta = 0$ in Fig. 5(a), and their closer view in (b). The twelve Dirac cones are arranged on a circle with a radius $\Delta k = 4(2 - \sqrt{3})\pi/(3a)$, and they are strongly hybridized near $\mathbf{k}_0 = \mathbf{0}$ with $t_0 = 0.0465 V_{pp\pi}^0$ to exhibit the characteristic dispersion including flat band bottoms, the Mexican-hat edges, and the filled band edges. We can get the electronic structures of various dodecagonal vdW-QCs by using the proper $V_{pp\pi}^0$; e.g.,

$V_{pp\pi}^0 = -3.38 \text{ eV}$ [24] gives the spectrum of vdW-QC composed of two graphene layers, which is known as quasicrystalline twisted bilayer graphene.

At $\mathbf{k}_0 = \mathbf{0}$, $\mathcal{H}_{\text{ring}}$ can be analytically diagonalized to obtain a set of energies (neglecting the constant energy)

$$E_m^\pm = t_0 \cos q_m \pm \sqrt{3t_0^2 \sin^2 q_m + (h_0 - 2t_0 \cos q_m)^2}, \quad (25)$$

where $h_0 \equiv h_{AB}(\mathbf{Q}_0) = h_{BA}(\mathbf{Q}_0) = -0.682 V_{pp\pi}^0$, and $q_m = (7\pi/6)m$ with $m = -5, -4, \dots, 5, 6$ is the wave number along the chain. Unlike the octagonal vdW-QCs in the minimal model (Sec. III A), which has one set of the hybridized states, the dodecagonal vdW-QCs show hybridization both in the conduction band and valence bands, which correspond to \pm in Eq. (25), respectively. The energy scaling in the conduction band is, however, much smaller than that in the valence band since the wave function of the conduction band of the hexagonal lattices, having the same phases between the sublattices, suppresses the interlayer interaction by a factor of 3. The index m is a quantized angular momentum respecting the 12-fold rotational symmetry. The states with $m = \pm s$ ($s = 1, 2, 3, 4, 5$) form twofold doublets, while the $m = 0$ and 6 are non-degenerate. Note that the interaction responsible for the formation of the quasicrystalline states only weakly affects the spectrum at energies away from the momentum matching conditions; e.g., in a quasicrystalline twisted bilayer graphene there is no meaningful change on the Fermi velocity [2], since E_m^\pm are far from the Dirac point.

Figure 5(c) shows the LDOS of the quasicrystalline states, where we can see that the wave amplitude distribute selectively on a limited number of sites in a characteristic 12-fold rotationally symmetric pattern. The wave functions for E_m^\pm are $\mathbf{v}_m^\pm = (1/\sqrt{12})(\mu_m^{-5}, \mu_m^{-4}, \mu_m^{-3}, \dots, \mu_m^6) \otimes (c_{m,1}^\pm, c_{m,2}^\pm)$ ($\mu_m = e^{iq_m}$), where $(c_{m,1}^+, c_{m,2}^+) = (\sin(\phi_m/2), \cos(\phi_m/2))$ and $(c_{m,1}^-, c_{m,2}^-) = (\cos(\phi_m/2), -\sin(\phi_m/2))$ are the coefficients of the sublattices arranged in the order of the bases of Eq. (20), and $\phi_m = \tan^{-1}[(h_0 - 2t_0 \cos q_m)/(\sqrt{3}t_0 \sin q_m)]$. Since the Hamiltonian has a symmetry of

$$\begin{aligned} \Sigma'^{-1} \mathcal{H}_{\text{ring}} \Sigma &= \mathcal{H}_{\text{ring}}^* \\ \Sigma &= \text{diag}(\sigma_x, \sigma_x, \sigma_x, \sigma_x, \sigma_x, \sigma_x) \end{aligned} \quad (26)$$

at $\mathbf{k}_0 = \mathbf{0}$, the states with angular momentum m and $-m$ are degenerate and $\mathbf{v}_{-m}^\pm = \sigma_x(\mathbf{v}_m^\pm)^*$, and it is straightforward to show that their LDOS profiles are exactly the same to each other. Figure 5(c) also shows that the states with $\pm m$ exhibit LDOS profiles which look similar to those of $6 \mp m$; the analysis on the wave functions \mathbf{v}_m^\pm clearly shows that the states with $m = 0$ and 6, and also the states with $m = 3$ and -3 have LDOS that are exactly the same as each other, while the LDOS profiles of the other states (i.e., $m = \pm 1$ and ± 5 , and also $m = \pm 2$ and ± 4) become different as $|t_0|$ grows. Likewise, the

$\pm m$ states in the conduction band exhibit LDOS profiles which look similar to the $3 \mp m$ ones in the valence band in the systems with a small $|t_0/V_{pp\pi}^0|$.

3. The effect of the interlayer interaction and 12- and 2-wave mixing

Figure 6(a) shows the valence band structures of a dodecagonal vdW-QC with an interlayer interaction $t(\mathbf{q})$ that is 2 times larger than the one in Fig. 5. The energy spacing between the quasicrystalline states becomes larger, and the flat band area of $m = 6$ ($m = \pm 4$) state in the valence band in Fig. 6(a) is approximately 2-times (5-times) as large as that in Fig. 5(a), and it is 28-times (70-times) bigger than the flat band area of magic-angle twisted bilayer graphene. As a greater number of the electronic states are involved in the flat bands, we expect to see stronger electron-electron interacting effect. The density map in Fig. 6(b) shows the DOS of dodecagonal vdW-QCs with various t_0 calculated by using 182-wave bases. The white dashed line corresponds to the DOS for the system considered in Fig. 5, and the black dashed lines show the band edges of the quasicrystalline states [Eq. (25)].

The systems with larger $|t_0|$ exhibit higher DOS peaks owing to the increase of the flat band area in the momentum space. Not every quasicrystalline state leads to a DOS displaying spiky peaks interspersed with pseudogaps, so quasicrystalline features would be most prominent at the energies where the band edges coincide with the spiky peaks in DOS, especially at the $m = 6, \pm 4, \pm 3$ states in the valence band and the $m = 6, \pm 1, \pm 4$ states in the conduction band. Again, changing t_0 neither changes the symmetry nor degeneracy of quasicrystalline states. In most practical parameter ranges, a system with larger $|t_0|$ exhibits a larger energy spacing between the quasicrystalline states in both the conduction and valence bands. Note that, in the systems with extremely strong interlayer interaction ($|t_0| > h_0/2$), the energy spacing in the conduction band may decrease as $|t_0|$ increases (Appendix C). Such a condition, however, is hard to be achieved in the most practical systems. Thus, hereafter, we will consider the systems with $|t_0| < h_0/2$ only.

In addition to the quasicrystalline 12-wave mixing, Fig. 6(b) shows the features from the 2-wave mixing. The two DOS peaks and the dips in between, which originate at $E = -0.5 |V_{pp\pi}^0|$ when $t_0 = 0$, show the band edges and pseudogaps arising from intralayer 2-wave mixing [5, 8, 22]. We plot the band opening associated the interlayer and intralayer mixing as the blue and red arrows in Figs. 5(a) and 6(a), respectively, and visualize these interactions in Fig. 6(c). The band opening by the 2-wave mixing in the conduction band is much smaller than that in the valence band for the same reason as the band opening via the 12-wave mixing (Sec. III B 2). Although the interlayer interaction strength $t(\mathbf{q})$ involved in the intralayer 2-wave mixing is about 1.50 times the

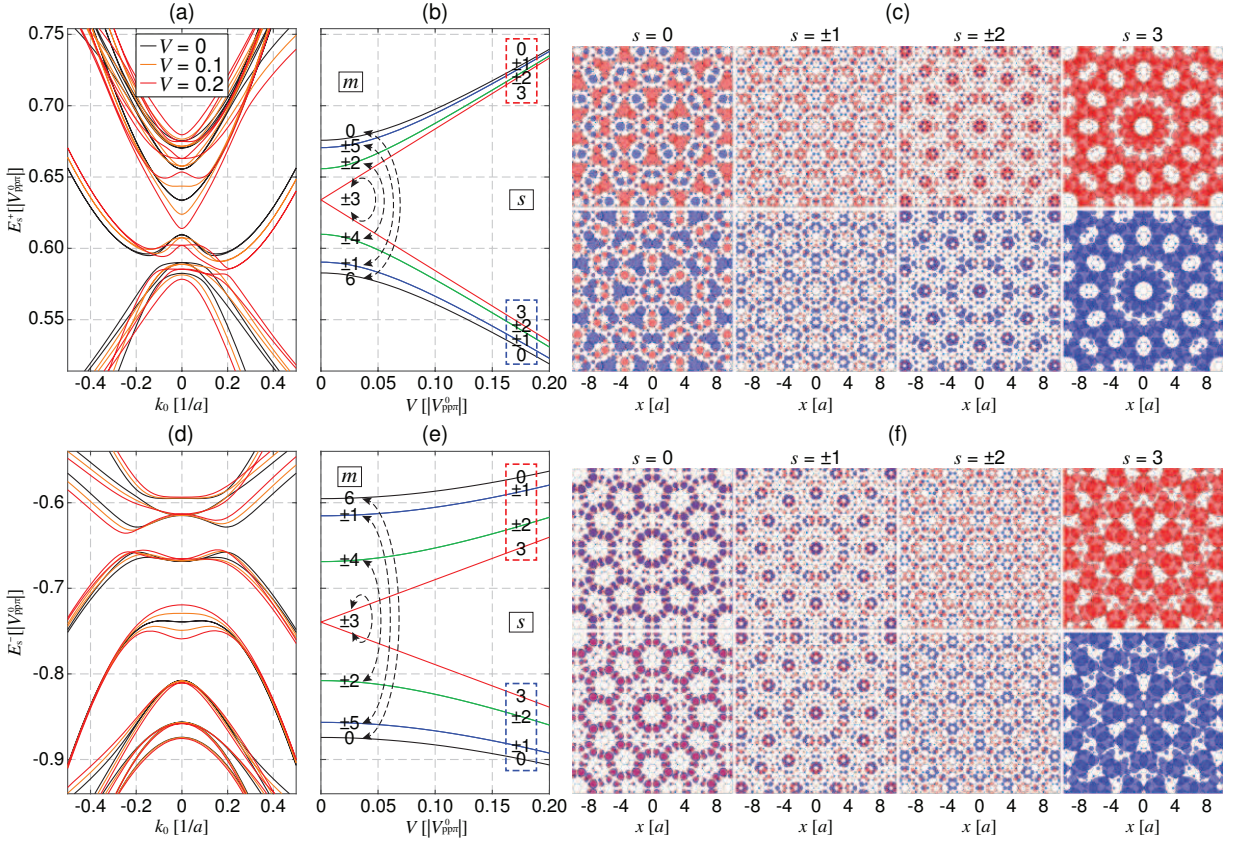


FIG. 7. (a) Conduction band dispersion near \mathbf{C}_n of dodecagonal vdW-QCs under three different interlayer potential asymmetry values, $V = 0, 0.1 |V_{pp}^0|, 0.2 |V_{pp}^0|$. (b) Conduction band edges at \mathbf{C}_n with various V . Indices m and s show the angular momentum of the pristine quasicrystalline states with 12-fold rotational symmetry and that of 6-fold rotational symmetry under interlayer potential asymmetry. Dashed arrows show the interaction between the constituent quasicrystalline states by \mathcal{H}_V . (c) Plots similar to Fig. 5(c) for $V \neq 0$ in the conduction band. The top and bottom panels show the LDOS of the upper and lower bands, respectively. (d), (e), (f): Plots similar to (a), (b), (c) for valence band.

interaction strength in the interlayer 2-wave mixing, the intralayer mixing exhibits smaller band opening since it involves two successive interlayer interaction between the states with different energies. At sufficiently large $|t_0|$ ($> 0.08 |V_{pp}^0|$), however, the intralayer interaction gives band opening throughout the entire Brillouin zone in the valence band except in the vicinity of the quasicrystalline states. This means that the quasicrystalline states with $m = 6, \pm 1$ are easily observable in the specific energy window where the quasicrystalline states remain after the weakly coupled bands become gapped. At $t_0 \rightarrow 0$ limit, the interlayer 2-wave mixing emerges at an energy that is the same as the 12-wave mixing, while the intralayer 2-wave mixing emerges at an energy much closer to $E = 0$. Again, the states and band opening arising from these three different mixings are continuously connected to each other in the Brillouin zone [Figs. 6(a) and (c)]. The 2-wave mixing can occur in bilayer hexagonal lattices stacked at any rotation angle θ , but α and β occur at different energies when $\theta \neq 30^\circ$.

4. Effects of interlayer potential asymmetry

Figures 7(a) and (d) show the dispersion in the conduction band and valence band near \mathbf{C}_n of dodecagonal vdW-QCs under three different interlayer asymmetric potential, $V = 0, 0.1, 0.2$ in units of $|V_{pp}^0|$. Again, the states with $m = \pm 3$ at $\mathbf{k}_0 = \mathbf{0}$ lose their degeneracy and all of the band edges, in both the conduction band and valence band, move away from $E_{m=\pm 3}$ as V increases.

At $\mathbf{k}_0 = \mathbf{0}$, the interlayer potential asymmetry couples the eigenstates of $\mathcal{H}_{\text{ring}}$, \mathbf{v}_m^b (b is $+$ for conduction band and $-$ for valence band), whose angular momenta differ by ± 6 ,

$$\begin{aligned} & \langle \mathbf{v}_{m'}^{b'} | \mathcal{H}_V | \mathbf{v}_m^b \rangle \\ &= \begin{cases} -\frac{V}{2} (c_{m',1}^{b'} c_{m,1}^b + c_{m',2}^{b'} c_{m,2}^b) & (m - m' \equiv 6 \pmod{12}) \\ 0 & (\text{otherwise}), \end{cases} \end{aligned} \quad (27)$$

since the diagonal elements of \mathcal{H}_V work as a staggered potential with $1/6$ period of the ring in the dual tight-binding lattice. Thus, the Hamiltonian matrix is reduced

to six 4×4 matrices

$$\begin{aligned} \tilde{\mathcal{H}}_{m,m'} &= \begin{pmatrix} C_m & -\frac{V}{2}R(\frac{\phi_m - \phi_{m'}}{2}) \\ -\frac{V}{2}R^{-1}(\frac{\phi_m - \phi_{m'}}{2}) & C_{m'} \end{pmatrix}, \\ C_m &= \begin{pmatrix} E_m^- & 0 \\ 0 & E_m^+ \end{pmatrix}, \end{aligned} \quad (28)$$

in the bases of $(\mathbf{v}_m^-, \mathbf{v}_m^+, \mathbf{v}_{m'}^-, \mathbf{v}_{m'}^+)$ for $(m, m') = (0, 6), (1, -5), (2, -4), (3, -3), (4, -2), (5, -1)$, where $R(\phi)$ is a rotation matrix. The electronic states lose the 12-fold rotational symmetry, since \mathcal{H}_V lifts the degeneracy of $|\mathbf{k}^{(n)}\rangle$ in different layers, and are characterized by the angular quantum number $s (= 0, \pm 1, \pm 2, 3) \equiv m \equiv m' \pmod{6}$ for a 6-fold rotational symmetry. We obtain two band edges E_s^+ in the conduction band and another two E_s^- in the valence band by diagonalizing Eq.(28). These are plotted against V in Figs. 7(b) and (e), for the conduction and valence bands, respectively. It is straightforward to show that the states with a quantum number s and $-s$ ($s = 1, 2$) are degenerate, since the reduced Hamiltonian satisfies

$$\begin{aligned} \tilde{\Sigma}^{-1} \tilde{\mathcal{H}}_{m,m'} \tilde{\Sigma} &= \tilde{\mathcal{H}}_{-m, -m'}, \\ \tilde{\Sigma} &= \text{diag}(1, -1, 1, -1). \end{aligned} \quad (29)$$

In most practical cases, Eq.(28) can be further reduced to two 2×2 matrices, since the interaction between the state in the conduction band and the state in valence band is almost negligible. This is partly due to the large energy difference and partly due to $(\phi_m - \phi_{m'})/2 \approx 0$ (since $\phi_m \approx \phi_{m'} \approx 90^\circ$).

The dashed arrows in Figs. 7(b) and (e) show the interaction between quasicrystalline states between \mathbf{v}_m^\pm and $\mathbf{v}_{m'}^\pm$ by \mathcal{H}_V . The states in the conduction band exhibit larger mixing between the constituent quasicrystalline states than those in the valence band, due to the smaller energy difference (not shown). And, similar to the octagonal vdW-QCs [Fig. 4(c)], materials with weaker $|t_0|$ under larger V experience larger energy shift, mixing, and accordingly larger spatial layer-polarization because of Eq. (19) (Appendix D). Again, the states with $s = 3$ are special in that the constituent states $\mathbf{v}_{m=3}^\pm$ and $\mathbf{v}_{m=-3}^\pm$ are always fully mixed regardless of the values of t_0 and V , due to the degeneracy between $E_{m=3}^\pm$ and $E_{m=-3}^\pm$.

We plot the LDOS of the states in the conduction band and valence band with $s = 0, \pm 1, \pm 2, 3$ at $V = 0.2 |V_{pp\pi}^0|$ in Figs. 7(c) and (f), respectively, where the top and bottom panels in each figure show the LDOS of the upper and lower bands, respectively. Again, the stronger the mixing, the more the wave functions are layer polarized, and the wave functions $\Psi_{s=3}^\pm$ are mostly polarized to either layer even at very weak V . The LDOS profile of each layer-polarized state is exactly consistent with the profile of each layer in the absence of the potential asymmetry [Fig. 5(c)], since \mathcal{H}_V does not change the Umklapp scattering paths.

In dodecagonal vdW-QCs with sublattice symmetry (i.e., $\Delta = 0$), an interlayer potential asymmetry does not

open a gap at the Dirac point. This is because the coexistence of the time reversal symmetry and the in-place C_2 rotation symmetry requires vanishing of the Berry curvature at any nondegenerate point the the energy band [23], and this guarantees the robustness of band touching points in two-dimensional systems [25]. Just like twisted bilayer graphene with any rotation angle [10], dodecagonal vdW-QCs composed of two hexagonal lattices with $\Delta = 0$ has the C_2 symmetry, even in the presence of interlayer potential asymmetry because C_2 does not flip the layers. Thus, the Dirac points of dodecagonal vdW-QCs with $\Delta = 0$ are protected even in the presence of interlayer potential asymmetry.

5. Effects of sublattice potential asymmetry

We plot the conduction band and valence band near \mathcal{C}_n of a dodecagonal vdW-QC with sublattice potential asymmetry of $\Delta = -0.60 V_{pp\pi}^0$ in Figs. 8(b) and (e), respectively, and plot the bands in the absence the asymmetry in (a) and (d) as a reference. $\Delta \neq 0$ in the current model makes a band opening as large as Δ at the energy range centered at $E = 0$. Unlike the interlayer potential asymmetry, however, we can see that breaking the sublattice symmetry does not make dramatic change to the band structures near the quasicrystalline states.

The potential which breaks the sublattice symmetry, \mathcal{H}_Δ , couples the eigenstates of $\mathcal{H}_{\text{ring}}$, \mathbf{v}_m^b , whose angular momenta differ by ± 3 ,

$$\begin{aligned} \langle \mathbf{v}_{m'}^b | \mathcal{H}_\Delta | \mathbf{v}_m^b \rangle &= \begin{cases} \frac{(1-i)\Delta}{4} (c_{m',1}^{b'} c_{m,1}^b - c_{m',2}^{b'} c_{m,2}^b) & (m - m' \equiv -3 \pmod{12}), \\ \frac{(1+i)\Delta}{4} (c_{m',1}^{b'} c_{m,1}^b - c_{m',2}^{b'} c_{m,2}^b) & (m - m' \equiv 3 \pmod{12}), \\ 0 & (\text{otherwise}), \end{cases} \end{aligned} \quad (30)$$

since the diagonal elements of \mathcal{H}_Δ work as a potential with $1/3$ period of the ring in the dual tight-binding lattice. Thus, \mathcal{H}_Δ couples quasicrystalline states with four different m , $(m_1, m'_1, m_2, m'_2) = (0, 3, 6, -3), (1, 4, -5, -2), (-1, 2, 5, -4)$, and the Hamiltonian matrix is reduced to three 8×8 matrices

$$\begin{aligned} \tilde{\mathcal{H}}_{m_1, m'_1, m_2, m'_2} &= \begin{pmatrix} C_{m_1} & \mathcal{D}_{m_1, m'_1} & 0 & \mathcal{D}_{m'_2, m_1}^\dagger \\ \mathcal{D}_{m_1, m'_1}^\dagger & C_{m'_1} & \mathcal{D}_{m'_1, m_2} & 0 \\ 0 & \mathcal{D}_{m'_1, m_2}^\dagger & C_{m_2} & \mathcal{D}_{m_2, m'_2} \\ \mathcal{D}_{m'_2, m_1} & 0 & \mathcal{D}_{m_2, m'_2}^\dagger & C_{m'_2} \end{pmatrix}, \\ \mathcal{D}_{m_a, m_b} &= \frac{(1+i)\Delta}{4} \begin{pmatrix} \cos \bar{\phi}_m & \sin \bar{\phi}_m \\ \sin \bar{\phi}_m & -\cos \bar{\phi}_m \end{pmatrix} \end{aligned} \quad (31)$$

in the bases of $(\mathbf{v}_{m_1}^-, \mathbf{v}_{m_1}^+, \mathbf{v}_{m_2}^-, \mathbf{v}_{m_2}^+, \mathbf{v}_{m'_1}^-, \mathbf{v}_{m'_1}^+, \mathbf{v}_{m'_2}^-, \mathbf{v}_{m'_2}^+)$, where $\bar{\phi}_m \equiv (\phi_{m_a} + \phi_{m_b})/2$. The electronic states lose the 12-fold rotational symmetry, and are characterized by the angular quantum number $s (= 0, \pm 1) \equiv m_i \pmod{3}$ ($m_i = m_1, m_2, m'_1, m'_2$) for a 3-fold rotational symmetry. Again, the states with a quantum number $s = 1$ and $s = -1$ are degenerate, due to the symmetry of the

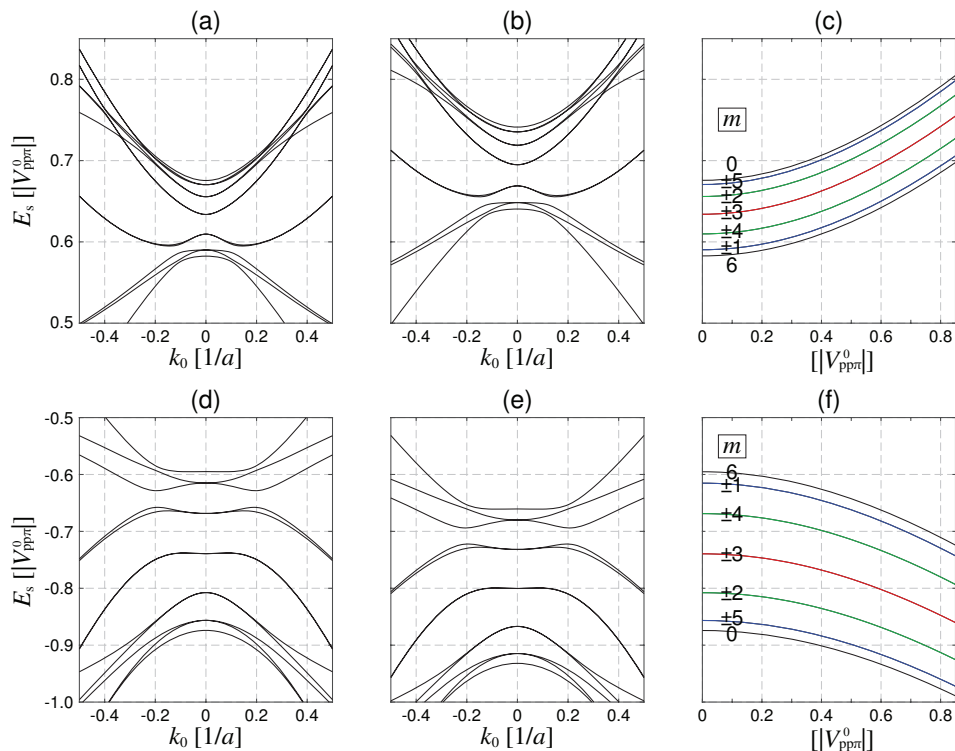


FIG. 8. (a) and (b): Conduction band dispersion near \mathbf{C}_n of a dodecagonal vdW-QC with sublattice potential asymmetry of (a) $\Delta = 0$ and (b) $-0.60 V_{pp\pi}^0$, respectively. (c) Band edges at \mathbf{C}_n with various Δ . Indices m show the angular momentum of the pristine quasicrystalline states with 12-fold rotational symmetry. (d), (e), (f): Plots similar to (a), (b), (c) for valence band.

Hamiltonian. And in most practical cases, Eq. (31) can be further reduced to four 2×2 matrices, since the interaction between the state in the conduction band and the state in valence band is almost negligible due to the large energy difference.

Figures 8(c) and (f) show the energies E_s^\pm in the unit of $|V_{pp\pi}^0|$ plotted against Δ . Unlike the interlayer potential asymmetry, Δ merely shifts the energies slightly away from the Dirac point and does not make dramatic change to the quasicrystalline states, which is consistent with the band structures in Figs. 8(b) and (e). This is because, $|c_{m,1}^b| \approx |c_{m,2}^b|$ in most practical systems with $|t_0| < h_0/5$ ($\phi_m \approx 90^\circ$) at this high energy regime. Thus, the potential, which has the opposite sign between the sublattices, is almost cancelled in the intraband interaction ($b = b'$), due to the phase cancellation. On the other hand, although materials with much higher $|t_0|$ have finite contribution from the sublattice phases in the intraband interaction, the overall interaction is still very weak since the energy difference between the quasicrystalline states increases as $|t_0|$ grows. In any system, the interband interaction ($b \neq b'$) is always negligible due to the large energy difference. Thus, a bilayer of hexagonal lattices with sublattice potential asymmetry stacked at 30° will also exhibit the quasicrystalline states and DOS analogous to the quasicrystals composed of bilayer graphene.

If the two layers have different Δ , other than a simple sign difference, the degeneracy of the $m = \pm 3$ states is lifted but the other states remain almost the same.

IV. CONCLUSIONS

We investigated the electronic structures of quasicrystals composed of the incommensurate stack of atomic layers (vdW-QCs) for every rotational symmetry possible in two-dimensional space. We show that the rotational symmetry of the quasicrystal as well as the translational symmetries of the constituent atomic layers give the quasicrystalline resonant coupling between the intrinsic states of the constituent layers. Furthermore, we reveal the emergence of the quasi-band dispersion and wave functions respecting the quasicrystalline order of each system. Although the quasicrystalline states coexist in energy with weakly coupled states (e.g., the states arising from the interaction which is typically known as *moiré interaction*) in general, we showed that some quasicrystalline states, which are usually obscured by additional weakly coupled states, are more prominent in quasicrystals with strong interlayer interaction.

From the analysis on the symmetry of the interlayer interaction, we show that even the atomic layers with differ-

ent types of orbitals will also exhibit the quasicrystalline states if all the dominant interlayer interaction occurs between the atomic orbitals having the same magnetic quantum number. In this sense, most of dodecagonal vdW-QCs including those composed of transition metal dichalcogenides will also clearly show the quasicrystalline states.

Besides, we investigate the effects of lifting both interlayer and sublattice symmetry on the electronic structures. Since the quasicrystalline order arises from the resonant interaction between the states in both layers, we can switch between the states fully respecting quasicrystal symmetry and those satisfying only half the symmetry by turning on and off the interlayer symmetry. We also analytically interpret the mixing between the quasicrystalline states, which may influence other physical properties such as optical selection rules. The quasicrystalline states in the middle are special in that they are always fully mixed and 100% layer polarized regardless of the magnitude of the interlayer asymmetry. On the other hand, we show that sublattice potential asymmetry in hexagonal lattices does not make a dramatic difference - it results only in a constant energy shift from the original quasicrystalline states.

This is the first theoretical work which investigated the formation of quasicrystalline states for every possible two-dimensional bilayer quasicrystal system, which will lead to extended exploration of rich quasicrystal physics in designer quasicrystals. In experiment, the quasicrystalline bands will be observed in Angle-resolved photoemission spectroscopy clearly at C_n then much weakly at other wave vectors including Γ by Umklapp scattering. Optical selection rule would be different from that of the constituent layers, and we can switch between the two different rules by switching on and off the interlayer potential asymmetry. And, unlike the moiré superlattices stacked at other angles, vdW-QCs will not show circular dichroism. Besides, scanning tunneling microscope will show the LDOS respecting the quasicrystalline tiling. In the most widely studied system, graphene quasicrystals, however, most quasicrystalline states coexist in energy with almost decoupled monolayer states. Thus, the quasicrystalline pattern of LDOS will be visible as a weak deviation from the uniform electron distribution or by exposing the states by increasing the interlayer interaction, e.g., by applying pressure, by intercalation of ions, or by addition of barrier atomic layers. Besides, the growth of the band flatness near C_n with respect to the increase of the interlayer interaction will significantly reduces the conductivity, and the electron-electron interaction in such flat bands may serve as the source of many interesting phenomena such as the enhancement of electron-phonon coupling.

Note added. During the completion of this work, we became aware of recent theoretical works on the pres-

sure and electric field dependence of quasicrystalline electronic states in 30° twisted bilayer graphene [26].

ACKNOWLEDGMENTS

This work was supported by Science and Technology Commission of Shanghai Municipality grant no. 19ZR1436400, and NYU-ECNU Institute of Physics at NYU Shanghai. This research was carried out on the High Performance Computing resources at NYU Shanghai.

Appendix A: Quasicrystalline states with weaker interaction

As mentioned in Sec. IID, the sets of the waves in Figs. 1(b) and (e) are not the only set of states which show a resonant coupling in each system. We can find more sets of states, with different wave numbers, showing the resonant interaction respecting the rotational symmetry of the quasicrystals. For example, the eight states \mathbf{k} (red) and $\hat{\mathbf{k}}'$ (blue) in Fig. 9(a) also form a circular chain in the dual tight-binding lattice. Note that $\hat{\mathbf{k}}$ for these states ($= \mathbf{0}$) is different from that for the states in Fig. 1(b). These states are mapped to \mathbf{k} (red) and $\hat{\mathbf{k}}$ (blue) in the first Brillouin zone, experience a resonant interaction, and form quasicrystalline states. Figure 9(c) shows the band structures near the quasicrystalline states arising from these eight states. It should be noted that, however, the strength of the resonant interaction, $|t(\mathbf{q})|$, for the states in Fig. 9(a) is much weaker than that for the states in Fig. 1(b). This is because $|t(\mathbf{q})|$ decays fast as $|\mathbf{q}|$ grows, and the former states have the chain with a longer segment length ($=|\mathbf{q}|$). Thus, the band opening in Fig. 9(c) is much smaller than that in Figs. 2(a) and (b). Dodecagonal vdW-QCs also have more sets of states showing the resonant interaction. In most systems, however, such states can be mostly neglected since their interaction strengths are very weak, and they are also mixed with other types of interaction (e.g., 2-wave mixing). Thus, the sets in Figs. 1(b) and (e) give the strongest interaction, i.e., largest energy separation and clear quasicrystalline order, since these states form the rings with the shortest distance between neighboring states in the dual tight-binding lattices.

Appendix B: Particle-hole symmetry of the Hamiltonian of octagonal quasicrystal

By considering only the nearest neighbor pairs in the intralayer interaction, the ring Hamiltonian $\mathcal{H}_{\text{ring}}$ of the octagonal vdW-QCs [Eq.(13)], up to the first order to $\mathbf{k}_0 = (k_{0,x}, k_{0,y})$, can be transformed to

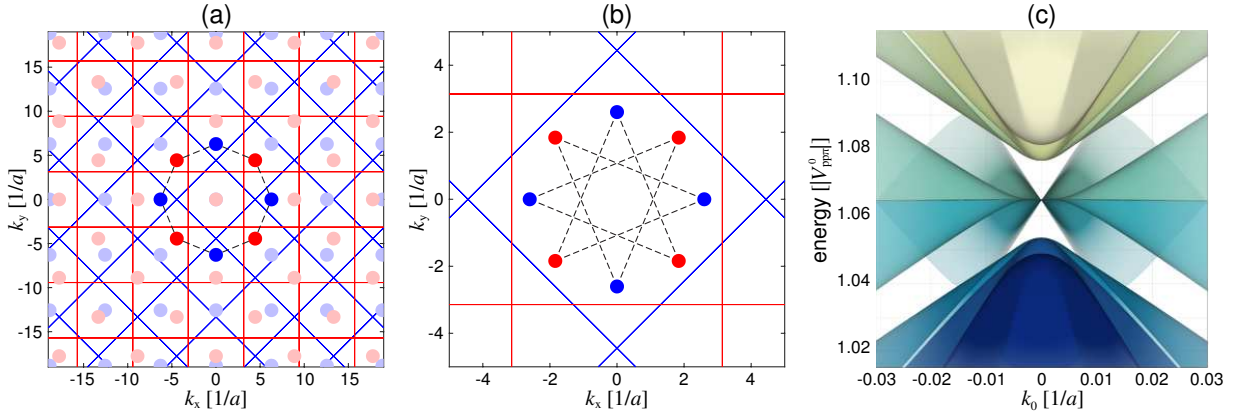


FIG. 9. (a) and (b) Plots similar to Figs. 1(b) and (c) for the next strongest quasicrystalline interaction in octagonal vdW-QCs, where $\hat{\mathbf{k}} = \mathbf{0}$. (c) Electronic structures near the second dominant quasicrystalline states of octagonal vdW-QCs calculated by the 8-ring effective model.

$$U^{-1}\mathcal{H}_{\text{ring}}(\mathbf{k}_0)U = \mathcal{H}'_{\text{ring}}(\mathbf{k}_0) = \begin{pmatrix} H^{(-3)} & C^* & & & C \\ C & H^{(-2)} & C^* & & \\ & C & H^{(-1)} & C^* & \\ & & \ddots & \ddots & \ddots \\ & & & C & H^{(3)} & C^* \\ C^* & & & & C & H^{(4)} \end{pmatrix} \quad (\text{B1})$$

with a transformation matrix

$$U = (\mathbf{v}_{-3}, \mathbf{v}_{-2}, \mathbf{v}_{-1}, \dots, \mathbf{v}_3, \mathbf{v}_4), \quad (\text{B2})$$

where $\mathbf{v}_m = \frac{1}{\sqrt{8}}(\mu_m^{-3}, \mu_m^{-2}, \dots, \mu_m^3, \mu_m^4)^T$ ($\mu_m = e^{i5\pi m/4}$) is the eigenstate of the quasicrystalline state with a quantized angular momentum of m , $H^{(m)} = h_0 - 2t_0 \cos(5\pi m/4)$, and $C(\mathbf{k}_0) = \sin(\sqrt{2}\pi)aV_{pp\pi}^0(k_{0,x} - ik_{0,y})$. Then, it is straightforward to show that $\mathcal{H}'_{\text{ring}}$ has a particle-hole symmetry with respect to the energy $E = h_0$,

$$\begin{aligned} \Sigma^{-1}(\mathcal{H}'_{\text{ring}} - h_0\mathbb{I})\Sigma &= -(\mathcal{H}'_{\text{ring}} - h_0\mathbb{I}), \\ \Sigma &= \begin{pmatrix} & & \sigma_z & & \\ & & & \sigma_z & \\ \sigma_z & & & & \\ & \sigma_z & & & \end{pmatrix}, \end{aligned} \quad (\text{B3})$$

where \mathbb{I} is an 8×8 unit matrix. This immediately demonstrates that if $\Psi(\mathbf{k}_0)$ is an eigenstate of $\mathcal{H}'_{\text{ring}}$ with an energy of $h_0 + E$, then $\Sigma^{-1}\Psi(\mathbf{k}_0)$ is an eigenstate of energy $h_0 - E$.

Appendix C: Band edges of quasicrystalline states of dodecagonal vdW-QCs with various t_0

Figure 10 shows the band edges of quasicrystalline states of dodecagonal vdW-QCs [Eq. (25)] with various

interlayer interaction strength t_0 up to the strong interaction regime. We can see that the energy spacing between the quasicrystalline states increases as $|t_0|$ increases in most practical interaction strength, i.e., $|t_0| < h_0/2$ ($h_0 = -0.682 V_{pp\pi}^0$), while the energy spacing in the conduction band decreases as $|t_0|$ exceeds $h_0/2$.

Appendix D: Energies and wave functions of dodecagonal quasicrystal with interlayer potential asymmetry

Figures 7(b) and (e) show that the states with $s = 0$ determine the energy span of the resonant states in the presence of the interlayer potential asymmetry, in both the conduction band and valence band. Equation (28) shows the coupling between the quasicrystalline states with angular momentum m by interlayer potential asymmetry. In most practical cases, the matrix can be further reduced to two 2×2 matrices,

$$\tilde{\mathcal{H}}_{m,m'}^{\pm} = \begin{pmatrix} E_m^{\pm} & -V/2 \\ -V/2 & E_{m'}^{\pm} \end{pmatrix}, \quad (\text{D1})$$

for the conduction band ($\tilde{\mathcal{H}}_{m,m'}^+$) and valence band ($\tilde{\mathcal{H}}_{m,m'}^-$), since the interaction between the state in the conduction band and the state in valence band is almost negligible due to the large energy difference. For the cou-

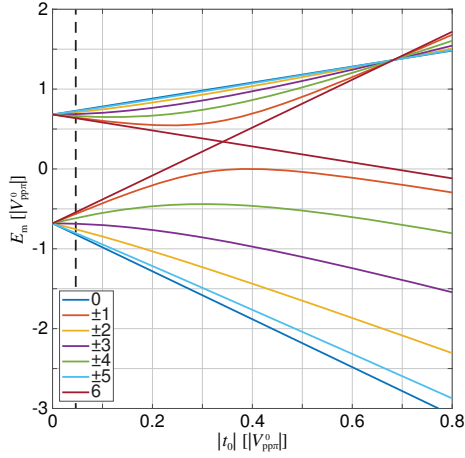


FIG. 10. Band edges of quasicrystalline states of dodecagonal vdW-QCs [Eq. (25)] with various interlayer interaction strength t_0 . The black dashed line corresponds to the band edges for the system considered in Fig. 5, and the numbers show the quantized angular momentum m .

pled states with $s = 0$ (i.e., $m = 0$ and $m' = 6$), the in-

teraction between the conduction band and valence band is completely forbidden due to the sublattice symmetry. Then, we get $E_{s=0}^- = -h_0 \pm \sqrt{9t_0^2 + V^2}/4$ in the valence band and $E_{s=0}^+ = h_0 \pm \sqrt{t_0^2 + V^2}/4$ in the conduction band, in the most practical systems with $|h_0| > 2|t_0|$. Thus, the states in the conduction band exhibit smaller energy span than those in the valence band.

The wave functions of the higher energy states in both the conduction band and valence bands are $\Psi_{s=0}^\pm = \sin(\tilde{\phi}/2)\mathbf{v}_{m=0}^\pm + \cos(\tilde{\phi}/2)\mathbf{v}_{m=6}^\pm$, and the lower energy states are $\Psi_{s=0}^\pm = \cos(\tilde{\phi}/2)\mathbf{v}_{m=0}^\pm - \sin(\tilde{\phi}/2)\mathbf{v}_{m=6}^\pm$, where $\tilde{\phi}$ is $\tan^{-1}(-V/(6t_0))$ for valence band and $\tan^{-1}(V/(2t_0))$ for conduction band. As $\tilde{\phi}$ becomes close to 90° , i.e., in materials with smaller $|t_0|$ and $|V| \gg |t_0|$, $\Psi_{s=0}^\pm$ becomes $(1/\sqrt{2})(\mathbf{v}_0^\pm + \mathbf{v}_6^\pm)$ for the upper state and $(1/\sqrt{2})(\mathbf{v}_0^\pm - \mathbf{v}_6^\pm)$ for the lower state. Since $\mathbf{v}_0^\pm = (1/\sqrt{24})(1, 1, 1, 1, \dots, 1) \otimes (1, \pm 1)$ and $\mathbf{v}_6^\pm = (1/\sqrt{24})(-1, 1, -1, 1, \dots, 1) \otimes (1, \pm 1)$, $\Psi_{s=0}^\pm$ becomes polarized to either layer, i.e., the state is mostly composed of the Bloch bases with n of even (layer 1) or odd (layer 2) numbers, in the systems with small interlayer interaction strength $|t_0|$. On the other hand, the states with $s = 3$ are always 100% polarized to either layer.

-
- [1] P. Stampfli, *Helv. Phys. Acta* **59**, 1260 (1986).
- [2] S. J. Ahn, P. Moon, T.-H. Kim, H.-W. Kim, H.-C. Shin, E. H. Kim, H. W. Cha, S.-J. Kahng, P. Kim, M. Koshino, Y.-W. Son, C.-W. Yang, and J. R. Ahn, *Science* **361**, 782 (2018).
- [3] T. Suzuki, T. Iimori, S. J. Ahn, Y. Zhao, M. Watanabe, J. Xu, M. Fujisawa, T. Kanai, N. Ishii, J. Itatani, *et al.*, *ACS Nano* **13**, 11981 (2019).
- [4] Y. Takesaki, K. Kawahara, H. Hibino, S. Okada, M. Tsuji, and H. Ago, *Chemistry of Materials* **28**, 4583 (2016).
- [5] W. Yao, E. Wang, C. Bao, Y. Zhang, K. Zhang, K. Bao, C. K. Chan, C. Chen, J. Avila, M. C. Asensio, *et al.*, *Proc. Natl. Acad. Sci.* **115**, 6928 (2018).
- [6] X.-D. Chen, W. Xin, W.-S. Jiang, Z.-B. Liu, Y. Chen, and J.-G. Tian, *Adv. Mater.* **28**, 2563 (2016).
- [7] S. Pezzini, V. Miseikis, G. Piccinini, S. Forti, S. Pace, R. Engelke, F. Rossella, K. Watanabe, T. Taniguchi, P. Kim, and C. Coletti, *Nano Lett.* **20**, 3313 (2020).
- [8] P. Moon, M. Koshino, and Y.-W. Son, *Phys. Rev. B* **99**, 165430 (2019).
- [9] J. C. Slater and G. F. Koster, *Phys. Rev.* **94**, 1498 (1954).
- [10] P. Moon and M. Koshino, *Phys. Rev. B* **85**, 195458 (2012).
- [11] G. Trambly de Laissardière, D. Mayou, and L. Magaud, *Nano Lett.* **10**, 804 (2010).
- [12] P. Moon and M. Koshino, *Phys. Rev. B* **87**, 205404 (2013).
- [13] E. J. Mele, *Phys. Rev. B* **81**, 161405 (2010).
- [14] R. Bistritzer and A. H. MacDonald, *Proc. Natl. Acad. Sci.* **108**, 12233 (2011).
- [15] M. Koshino, *New J. Phys.* **17**, 015014 (2015).
- [16] S. Aubry and G. André, Analyticity breaking and Anderson localization in incommensurate lattices, *Ann. Israel Phys. Soc* **3**, 18 (1980).
- [17] Z. Y. Zhu, Y. C. Cheng, and U. Schwingenschlögl, *Phys. Rev. B* **84**, 153402 (2011).
- [18] G.-B. Liu, W.-Y. Shan, Y. Yao, W. Yao, and D. Xiao, *Phys. Rev. B* **88**, 085433 (2013).
- [19] S. Fang, R. Kuate Defo, S. N. Shirodkar, S. Lieu, G. A. Tritsarlis, and E. Kaxiras, *Phys. Rev. B* **92**, 205108 (2015).
- [20] E. Cappelluti, R. Roldán, J. A. Silva-Guillén, P. Ordejón, and F. Guinea, *Phys. Rev. B* **88**, 075409 (2013).
- [21] G.-B. Liu, D. Xiao, Y. Yao, X. Xu, and W. Yao, *Chem. Soc. Rev.* **44**, 2643 (2015).
- [22] M. Koshino, P. Moon, and Y.-W. Son, *Phys. Rev. B* **91**, 035405 (2015).
- [23] P. Moon, Y.-W. Son, and M. Koshino, *Phys. Rev. B* **90**, 155427 (2014).
- [24] Note that the ratio between $V_{pp\sigma}^0$ and $V_{pp\pi}^0$ of the hexagonal lattices used in this work is different from that used in the previous works ($V_{pp\sigma}^0 \approx 0.48\text{eV}$ and $V_{pp\pi}^0 \approx -2.7\text{eV}$) on the twisted bilayer graphene [2, 11, 12] and graphene on hexagonal boron nitride [27]. In this work, we scaled $V_{pp\pi}^0$ by a factor of 1.25, while keeping $V_{pp\sigma}^0 \approx 0.48\text{eV}$, to compensate the deviation of the Fermi velocity of a pristine graphene due to the summation over sites in the hopping range and make the band dispersion and the energies of the van Hove singularities consistent with the experimental results [2, 5].
- [25] M. Koshino, *Phys. Rev. B* **88**, 115409 (2013).
- [26] G. Yu, M. I. Katsnelson, and S. Yuan, Pressure and electric field dependence of quasicrystalline electronic

states in 30° twisted bilayer graphene, arXiv preprint arXiv:2003.11879 (2020).

[27] P. Moon and M. Koshino, Phys. Rev. B **90**, 155406 (2014).